A local scattering approach for the effects of abrupt changes on boundary-layer instability and transition: A finite-Reynolds-number formulation for isolated distortions

ZhengFeng Huang [1,3] and Xuesong Wu[2,1]†

[1]Department of Mechanics, Tianjin University, Tianjin, 300072, China

[2]Department of Mathematics, Imperial College London, 180 Queen's Gate, London, SW7 2AZ, UK

[3]State Key Laboratory of Aerodynamics, China Aerodynamic Research and Development Center, Mianyang Sichuan, 621000, China

(Received xx; revised xx; accepted xx)

We investigate the influence of abrupt changes on boundary-layer instability and transition. Such changes can take different forms including local porous wall, suction/injection and surface roughness as well as junctions between rigid and porous walls. They may modify the boundary conditions and/or the mean flow, and their effects on transition have usually been assessed by performing stability analysis for the modified base flow and/or boundary conditions. However, such a conventional local linear stability theory (LST) becomes invalid if the change occurs over a relatively short scale comparable with, or even shorter than, the characteristic wavelength of the instability. In this case, the influence on transition is through scattering with the abrupt change acting as a local scatter, that is, an instability mode propagating through the region of abrupt change is scattered by the strong streamwise inhomogeneity to acquire a different amplitude. A local scattering approach (LSA) should be formulated instead, in which a transmission coefficient, defined as the ratio of the amplitude of the instability wave after the scatter to that before, is introduced to characterize the effect on instability and transition. In the present study, we present a finite-Reynolds-number formulation of LSA for isolated changes including a rigid plate interspersed by a local porous panel and a wall suction through a narrow slot. When the weak non-parallelism of the unperturbed base flow is ignored, the local scattering problem can be cast as an eigenvalue problem, in which the transmission coefficient appears as the eigenvalue. We also improved the method to take into account the non-parallelism of the unperturbed base flow, while it is found that the weak non-parallelism has a rather minor effect. The general formulation is specialized to two-dimensional Tollmien-Schlichting (T-S) waves. The resulting eigenvalue problem is solved, and full direct numerical simulations (DNS) are performed to verify some of the predictions by LSA. A parametric study indicates that conventional LST is valid only when the change is sufficiently gradual, and becomes either inaccurate or invalid when the scale of the local distortion is short. A local porous panel enhances T-S waves, while a local suction with a moderate mass flux significantly inhibits T-S waves. In the latter case, a comprehensive comparison is made between the theoretical predictions and experimental data, and a satisfactory quantitative agreement was observed.

Key words: Boundary layer stability; transition to turbulence; scattering; porous wall

† Email address for correspondence: x.wu@ic.ac.uk

1. Introduction

Instability and laminar-turbulent transition of boundary-layer flows remain an area of extensive research due to their fundamental importance in fluid physics and practical relevance for many technological applications. A boundary layer typically develops in the streamwise direction, giving rise to nonparallel-flow effects, which are weak in canonic situations. However, non-parallelism can be strong when the flow is subject to abrupt changes. Besides experimental methods, three main approaches have been taken to study instability and transition in boundary layers subject to different degree of non-parallelism, and these include: (i) Linear Stability Theory (LST), which amounts to solving eigenvalue problems (Reed *et al.* 1996), (ii) Method of Parabolized Stability Equations (PSE), which involves solving initial-boundary-value problems through marching downstream (Herbert 1997), and (iii) Direct Numerical Simulations (DNS), where one solves the full Navier-Stokes (N-S) equations as a time-dependent boundary-value problem. Recently, a local scattering approach (Wu & Dong 2016) was proposed to deal with strong non-parallelism that cannot be handled by either LST or PSE method. In order to put this relatively new approach in an appropriate context, we illustrate the key concepts and ideas of each approach using, for simplicity, a planar instability mode in a two-dimensional incompressible boundary layer as an example.

1.1. *Linear stability theory (LST)*

In LST, the base flow $\bar{\mathbf{Q}}$ is perturbed by a small disturbance $\mathbf{Q}'$ such that the instantaneous flow field $\mathbf{Q}$ is decomposed as

$$\mathbf{Q}(x, y, t) = \bar{\mathbf{Q}}(x, y) + \mathbf{Q}'(x, y, t), \tag{1.1}$$

where x and y denote the coordinates in the streamwise and wall-normal directions respectively in the Cartesian system (x, y), and t is the time variable. $\mathbf{Q}$ and $\bar{\mathbf{Q}}$ separately satisfy the N-S equations. On the assumption that the disturbance is of small amplitude, the linearized N-S equations are derived for $\mathbf{Q}'$. By making the local parallel-flow approximation, the disturbance $\mathbf{Q}'$ can be written in the form of a normal mode (Reshotko 1976),

$$\mathbf{Q}'(x, y, t) = \mathbf{q}(y) \exp[i(\alpha x - \omega t)] + c.c., \tag{1.2}$$

where ω and α denote the frequency and wavenumber of the perturbation respectively, the vector $\mathbf{q}$ characterizes its shape, and *c.c.* stands for complex conjugate. The disturbance equations can be simplified to the Orr-Sommerfeld (O-S) equation, which can be written as

$$L_0(\alpha, \omega; x)\, \mathbf{q} = \mathbf{0}, \tag{1.3}$$

where the operator L_0 contains differentiation with respect to y only; the dependence on x is parametric and may alternatively be viewed as on the local Reynolds number, $R = U_\infty^* \delta^* / \nu^*$, based on the boundary-layer (displacement) thickness δ^* with U_∞^* being the free-stream velocity and ν^* the kinematic viscosity. Equation (1.3) forms, along with the homogenous boundary conditions at the wall and infinity, an eigenvalue problem. A spatial stability problem is to find a complex eigenvalue $\alpha(\omega, x) = \alpha_r + i\alpha_i$ with a corresponding eigenfunction $\mathbf{q}$ for a given real ω and at a streamwise location x. For boundary layers, solutions of the O-S equation are referred to as Tollmien-Schlichting (T-S) waves, in which $-\alpha_i$ represents the spatial growth rate in the flow direction. A

disturbance is referred to as an amplifying (damped) mode if $-\alpha_i > 0$ (< 0). The flow is stable when $-\alpha_i < 0$ for all ω, and unstable when $-\alpha_i > 0$ for one or more ω. The condition $\alpha_i(\omega, x) = 0$ defines a neutral curve in the parameter space.

Once the local growth rate $-\alpha_i(\omega, x)$ is obtained by solving the eigenvalue problem at each location x, the so-called N-factor, which measures the accumulated growth of an instability mode with a given frequency ω, is calculated by integrating the growth rate with respect to x,

$$N = \ln \frac{A(x;\omega)}{A_0} = -\int_{x_0}^{x} \alpha_i(\omega, \xi) d\xi, \tag{1.4}$$

where $A(x;\omega)$ denotes the disturbance amplitude at an arbitrary downstream location x, whereas A_0 is the amplitude at the onset position x_0 of the instability, and its value is related to external disturbances and receptivity mechanisms. Without studying the latter, a commonly practiced engineering prediction tool is the so-called e^N-method, in which transition is deemed to occur when N reaches some critical value N_c, which is usually determined on an empirical basis.

Nonparallel-flow effects on linear stability have often been accounted for by a perturbative approach (Gaster 1974), which is applicable only when non-parallelism causes a small correction to the growth rate. Recently, a non-perturbative approach, free from this restriction, was proposed by Huang & Wu (2015).

1.2. *Method of the parabolized stability equations (PSE)*

An alternative, and now popular, method for studying instabilities in weakly nonparallel flows is the so-called PSE approach. By introducing a small parameter $\epsilon = O(R^{-1})$ and a slow variable $\xi = \epsilon x$, the disturbance $\mathbf{Q}'$ can be written as (Bertolotti *et al.* 1992)

$$\mathbf{Q}'(x, y, t) = \mathbf{q}(\xi, y) \exp[i(\alpha x - \omega t)] + c.c., \tag{1.5}$$

where $\mathbf{q}(\xi, y)$ is the shape function that varies slowly in the streamwise direction. Substitution of (1.5) into the disturbance equations yields, up to and including $O(\epsilon)$, the equations,

$$\Big(L_0(\alpha, \omega) + \epsilon L_0'(\alpha, \omega)\Big)\mathbf{q} + \epsilon L_1(\alpha, \omega)\frac{\partial \mathbf{q}}{\partial \xi} = 0, \tag{1.6}$$

where the operators L_0, L_0' and L_1 consist of derivatives with respect to y only, among which L_0 is the operator in LST, and L_0' and L_1 represent the contributions of the slow variations of the base flow and shape function respectively. Equations (1.6) are parabolic and are referred to as the Parabolized Stability Equations (PSE) since they involve only the first-order derivative with respect to the streamwise variable ξ. Nonlinear PSE approach, in which (1.5) consists of high harmonics, has also been developed. In addition to the boundary conditions at $y = 0$ and $y \to \infty$, the solution requires an initial condition at a starting position, which is often chosen to be a local eigen mode. The solution can be found by downstream marching.

The method of PSE accounts for the history of the disturbance (Herbert 1997). It has been developed into a fairly mature tool for predicting linear and nonlinear evolutions of two- and three-dimensional instability modes in weakly nonparallel shear flows including two- and three-dimensional, incompressible and compressible, boundary layers (Chang & Malik 1994; Malik *et al.* 1994; Herbert 1997). The predicted N-factor, or the amplitude A, may be used to estimate transition location by adopting a criterion based on a threshold N-factor N_c, or on a threshold amplitude A_c.

1.3. *Direct numerical simulation (DNS)*

DNS is another computational approach for studying instability and transition of boundary-layer flows (Kleiser & Zang 1991; Zhong & Wang 2012). The instantaneous flow field $\mathbf{Q}$, or the perturbation $\mathbf{Q}'$, is computed by numerically solving the full N-S equations. DNS resolves all time and length scales of the flow by using high-accuracy numerical methods and fine enough meshes. Computations could only be performed in a domain, which is a truncation of the flow field. Appropriate boundary conditions must be specified on the boundaries of the computational domain. Usually a collection of instability waves are imposed at the inlet to study their interactions and evolution. For boundary layers, an artificial numerical boundary condition at the outlet of the domain is specified in such a way that the upstream influence is prevented or kept minimal (Colonius 2004). Several such boundary conditions have been proposed including, e.g. the radiative boundary condition (Fasel 1976; Rist & Fasel 1995) and the absorbing boundary conditions (Kloker *et al.* 1993; Meitz & Fasel 2000; Bertolotti *et al.* 1992).

Using DNS, Worner *et al.* (2003) and Edelmann & Rist (2013) studied the effects of a step on an oncoming instability wave in an incompressible boundary layer, and Marxen *et al.* (2010) and Fong *et al.* (2013) investigated the impact of isolated roughness on first and second modes in a supersonic boundary layer. Xu *et al.* (2016) simulated the scattering of T-S waves on an incompressible boundary layer by isolated roughness elements, and quantified the destabilization effect in terms of the transmission coefficient first introduced by Wu & Hogg (2006).

1.4. *Local scattering problem (LSP) and local scattering approach (LSA)*

A canonical boundary layer may be subject to a certain local distortion, which may be caused, for example, by surface roughness/waviness, local suction or change of wall porosity or rigidity. If the distortion occurs over a length scale much longer than the wavelength of the inherent instability modes, a local stability analysis for the distorted mean flow and/or modified boundary conditions may still be justified. This is the approach that most previous studies took. Calculations of this kind were performed for local suction (Nayfeh & Reed 1985; Reed & Nayfeh 1986; Masad & Nayfeh 1992) and isolated roughness (Nayfeh *et al.* 1988; Cebeci & Egan 1989; Nayfeh & Abu-Khajeel 1996). The former is found to be stabilizing while the latter destabilizing. Linear and nonlinear PSE methods have been used to study effects of distributed roughness in the form of a wavy wall (Wie & Malik 1998; Park & Park 2013).

Local stability theory is valid provided that the distortion is gradual, i.e. it takes place over a length scale much longer than the characteristic length of the instability. However, when the distortion is abrupt in the sense that the former is comparable with, or even shorter than, the latter, the disturbance can no longer be expressed as a product of a slowly varying shape function and a fast carrier wave of the exponential form, that is, the normal mode assumption, which forms the very basis of LST and PSE, does not hold any more. Neither of them could be used to assess the influence of abrupt changes on instability and transition, which "needs to be investigated with more sophisticated methods" as Wie & Malik (1998) remarked. The appropriate methodology is to approach the problem from the perspective of a local scattering rather than local stability, as was first pointed out by Wu & Hogg (2006). In a Local Scattering Problem (LSP), an oncoming instability mode is scattered by the local inhomogeneity caused by the distortion, and the wave transmitted downstream acquires a different amplitude from what would be attained in the absence of the distortion. The ratio of the two is defined as the transmission coefficient, which provides a natural characterization of the overall

effect of the distortion on instability and transition. For the case of isolated roughness, a Local Scattering Approach (LSA) was formulated by Wu & Hogg (2006) using triple deck formalism, which assumes the Reynolds number to be asymptotically large.

While the physical concepts of local scattering and transmission coefficient are fairly general, the formulation and analysis of Wu & Hogg (2006) were restricted to a local roughness with a very small height that the local mean-flow distortion can be linearized. The case of a roughness with a height causing a nonlinear mean-flow distortion was considered by Wu & Dong (2016). They demonstrated that when the boundary-value problem governing the LSP is suitably discretized, the transmission coefficient appears as a generalized eigenvalue.

This paper presents a finite-Reynolds-number formulation of the local scattering approach. Compared with its high-Reynolds-number counterpart, a finite-Reynolds-number formulation is likely to be more accurate quantitatively and more accessible to investigators and users. The abrupt changes to be investigated are in the form of a finite porous panel interspersing a rigid wall and of a steady suction imposed through a narrow slot on the wall, but the formulation can easily be modified and extended to study other forms of abrupt distortions to two- and three-dimensional boundary layers. The length of the porous panel and suction slot is assumed to be comparable with the characteristic wavelength of the instability, and the length scale characterizing the adjustment of the porosity or the suction velocity is even shorter, leading to strong non-parallelism or inhomogeneity. Porosity influences only the unsteady disturbance through modifying the boundary condition, but not the base flow. In contrast, a suction causes an abrupt distortion to the base flow. The non-parallelism of the unperturbed base flow is weak, and is thus neglected in this investigation in order to focuss on the much stronger inhomogeneity associated with the local porosity and suction.

The rest of the paper is organized as follows. In §2, we give a general, but more detailed, description of LSP and LSA. A finite-Reynolds-number version of LSA is then formulated by specifying appropriate upstream and downstream conditions as well as the boundary conditions on the wall and at infinity. A simple dynamical model for a porous wall is described. This leads to a boundary-value problem governing the LSP. The numerical method for solving the boundary-value problem is described in §3. We show that when the weak non-parallelism is neglected, the problem leads to an eigenvalue problem, in which the transmission coefficient appears as the eigenvalue. The eigenvalue problem is solved to predict the disturbance development through the scattering zone as well as the transmission coefficient, and the results are presented in §4. We summarizes in §5 the main conclusions.

2. Problem description and formulation

2.1. *Description of the local scattering problem*

A typical local scattering problem is illustrated in figure 1 for the specific case of an isolated roughness element on an otherwise flat plate (Wu & Hogg 2006; Wu & Dong 2016). In general, the two flat portions of the boundaries are punctuated by a relatively small region of rapid variation, which causes short streamwise inhomogeneity. An oncoming (incident) instability mode, originated from the flat portion upstream (referred to as BC1), approaches the site of the local change, and is scattered by the streamwise inhomogeneity. In the region far downstream of the scatter (referred to as BC2), the disturbance relaxes to a local eigen mode, which will be referred to as the transmitted wave. Typical scatters include the following.

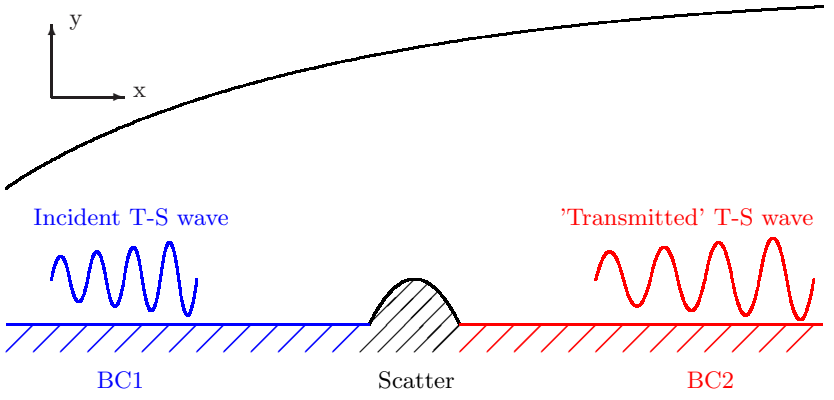

FIGURE 1. A diagrammatic illustration of a local scattering problem (LSP)

(i) Local roughness/wavy surface (Fujii 2006; Nayfeh *et al.* 1988; Cebeci & Egan 1989)
BC1/BC2 before/after the scatter are both rigid flat walls, between which a local roughness element is present. The shape of the roughness, $y = hF\big((x - x_c)/d\big)$, changes over on the scale d, which is assumed to be comparable with the wavelength, where x_c denotes the location of the roughness centre.

(ii) Local suction/injection or heating/cooling on the wall (Nayfeh & Reed 1985; Reynolds & Saric 1986; Reed & Nayfeh 1986; Masad & Nayfeh 1992; Masad 1995)
BC1 and BC2 are both rigid walls, and a steady suction/injection with a wall-normal velocity $\bar{v}\big((x - x_c)/d\big)$, or surface heating/cooling with a temperature $\bar{T}\big((x - x_c)/d\big)$, is applied on a finite section, whose length d is comparable with the wavelength.

(iii) Local porous/flexible surfaces (Wang & Zhong 2012)
BC1 and BC2 are both rigid walls, and they are joined by a porous or compliant section, where the unsteady normal velocity v', or the wall displacement f', is related to the pressure fluctuation p' on the surface.

(iv) Junction of a rigid wall with a semi-infinite porous/flexible surface
BC1 is a rigid wall, while BC2 is a porous/flexible surface, or vice versa. Here BC2 extends to infinity so that the junction acts a scatter.

We shall assume that (i) the base flow is steady, and the unsteady fluctuation is of small amplitude so that the linearized disturbance equations are valid in the whole domain, and (ii) the scatter is local, whose width d in the streamwise direction is comparable with the characteristic wavelength of the instability of the unperturbed flow. It follows that even though the disturbances far upstream and downstream are local eigen modes, the fluctuation near the scatter is not and can indeed be rather complex.

The impact of these abrupt distortions on instability and transition will be investigated in the framework of LSA, the key concept of which is the transmission coefficient (Wu & Hogg 2006). Its definition is illustrated in figure 2. Suppose that an incident instability wave, with an initial amplitude A_0 at position x_0 say, propagates downstream. Sufficiently upstream of the roughness element centred at x_c, the amplitude A_s of the instability wave evolves according to LST (as indicated by the dotted line), but in the vicinity of the roughness A_s deviates from that predicted by LST, and follows instead the solid curve in the figure. Sufficiently downstream, the disturbance relaxes to a local instability mode and is thus referred to as the transmitted instability wave. Let A_n denote the amplitude at position x_n and α_T denote the local eigenvalue in the far downstream region *in the absence of the scatter* (a region of rapid variation or a junction). Using A_n and α_T, one

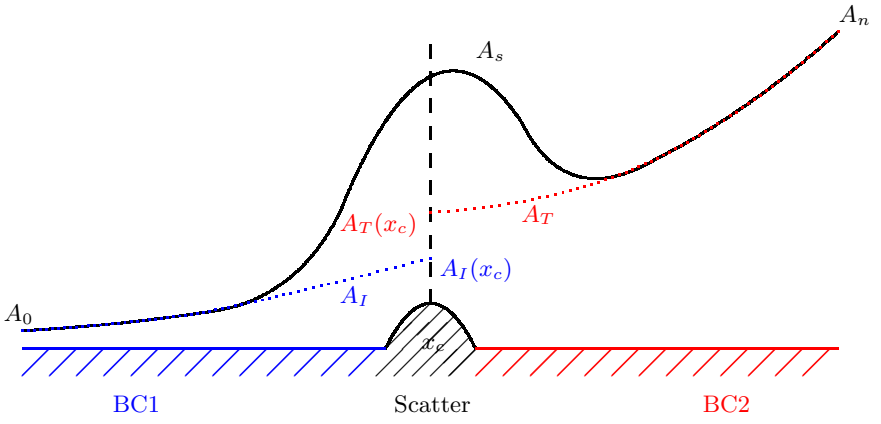

FIGURE 2. A diagrammatic illustration of local scattering and transmission coefficient $Tr = A_T(x_c)/A_I(x_c)$, where x_c is the center of the scatter, A_s the amplitude of disturbance in the presence of the scatter, whereas A_I and A_T represent the evolution and extrapolation of the incident and transmitted waves respectively in the absence of a scatter.

may extrapolate an effective initial amplitude $A_T(x_c)$ at x_c,

$$A_T(x_c) = A_n \exp\{-i \int_{x_c}^{x_n} \alpha_T(x) dx\}, \tag{2.1}$$

which is referred to as the amplitude of the transmitted wave. Note however that $A_T(x_c)$ is not the amplitude of the physical disturbance at x_c, i.e. $A_T(x_c) \neq A_s(x_c)$, but it is $A_T(x_c)$ that is important and relevant as will become clear later. On the other hand, if the scatter were absent, the upstream instability mode would have evolved according to LST (indicated by the dotted line in figure 2) to acquire an amplitude at x_c,

$$A_I(x_c) = A_0 \exp\{i \int_{x_0}^{x_c} \alpha_I(x) dx\}, \tag{2.2}$$

where α_I denotes the local eigenvalue in the far upstream region *in the absence of the scatter*, and $A_I(x_c)$ defines the 'amplitude of the incident wave'.

The transmission coefficient is then defined as (Wu & Hogg 2006)

$$Tr = A_T(x_c)/A_I(x_c). \tag{2.3}$$

In the absence of a scatter, $A_T(x_c) = A_I(x_c)$. It follows that the transmission coefficient provides a natural characterization of the impact of the scatter on stability and transition: the scatter suppresses the instability wave and hence delays transition if $|Tr| < 1$, but enhances the instability wave and boosts transition if $|Tr| > 1$.

The introduction of Tr based on $A_T(x_c)$ is convenient because it encapsulates the effect of the scatter and thereby allows LSA to be linked naturally with existing transition prediction methods for canonical boundary layers as follows. Use LST or PSE to describe the evolution of the instability wave upstream of the scatter and to obtain $A_I(x_c)$. Then using Tr, one finds $A_T(x_c) = TrA_I(x_c)$. With this $A_T(x_c)$ as the initial condition, LST or PSE can again be employed to predict the equivalent development far downstream of the scatter. With the aid of Tr, the development of the disturbance in the presence of a scatter is converted into an equivalent one without the scatter.

Before presenting a detailed mathematical formulation of LSA, we first highlight its key features and the main difference from LST and PSE. As in previous studies (Wu &

Hogg 2006; Wu & Dong 2016), it suffices to consider a wave with a given frequency ω since the disturbance is assumed to be small. We may write $\mathbf{Q}'$ in the form

$$\mathbf{Q}'(x, y, t) = \mathbf{q}(x, y) \exp(-i\omega t) + c.c. \tag{2.4}$$

It is important to point out that unlike the shape function (1.2) or (1.5) in LST and PSE respectively, the streamwise variation of $\mathbf{q}$ in (2.4) is on the short scale, comparable with the wavelength of the oncoming instability mode. Substituting (2.4) into the N-S equations and linearizing about the steady base flow, we obtain the equations for $\mathbf{q}(x, y)$, which form, along with appropriate boundary conditions including the upstream and downstream conditions, a boundary-value problem that is elliptic in its nature. The ansatz (2.4) looks similar to that in global stability analysis in that both allow for fast variation with x. The differences and relation between the two are worth noting. The first difference is that the frequency ω in the present work is real and given, as opposed to being a generally complex-valued eigenvalue to be found in the global stability problem. The second difference is that discrete global modes are usually assumed to be localized, i.e. attenuate in both the upstream and downstream directions, while the disturbances in the present scattering problem amplify downstream. On the basis of the last observation, the disturbance in the scattering problem may be viewed as a continuous neutral global mode.

For instability modes of the T-S type, the frequency $\omega \neq 0$. However, we may set $\omega = 0$ in the formulation if time-independent instability waves are considered, such as stationary crossflow vortices arising in three-dimensional boundary layers subject to a pressure gradient. Scattering of pre-existing vortices by two- and/or three-dimensional scatters can be analyzed in the same framework. Furthermore, by setting the amplitude of the upstream mode to zero ($A_I = 0$), the mathematical framework may also be used to compute the amplitude of the crossflow vortices excited by streamwise compact and spanwise periodic roughness elements (Choudhari & Duck 1996; Kurz & Kloker 2014).

2.2. *Governing equations*

The formulation of LSA will be given for a general three-dimensional incompressible boundary layer that develops over a nominally flat surface. The flow is described in the Cartesian coordinates (x^*, y^*, z^*), in which the surface is located at $y^* = 0$ with its leading edge at $x^* = 0$ and the x^* axis pointing to the downstream direction, while z^* is in the spanwise direction. Let $U^*_\infty, \rho^*_\infty$ and μ^*_∞ denote the free-scream velocity, density and viscous coefficient respectively with the superscript $*$ indicating a dimensional quantity. The reference length and time are taken to be δ^* and δ^*/U^*_∞ respectively, where δ^* is the displacement thickness of the boundary layer at a typical streamwise location. The resulting dimensionless coordinates and time variable will be denoted as (x, y, z) and t respectively. The velocity and pressure are normalized by U^*_∞ and $\rho^*_\infty U^{*2}_\infty$ respectively, and the corresponding non-dimensional quantities are denoted by (u, v, w) and p. The dimensionless three-dimensional incompressible N-S equations read

$$\frac{\partial u}{\partial x} + \frac{\partial v}{\partial y} + \frac{\partial w}{\partial z} = 0, \tag{2.5}$$

$$\frac{\partial u}{\partial t} + u\frac{\partial u}{\partial x} + v\frac{\partial u}{\partial y} + w\frac{\partial u}{\partial z} = -\frac{\partial p}{\partial x} + \frac{1}{R}\Big(\frac{\partial^2 u}{\partial x^2} + \frac{\partial^2 u}{\partial y^2} + \frac{\partial^2 u}{\partial z^2}\Big), \tag{2.6}$$

$$\frac{\partial v}{\partial t} + u\frac{\partial v}{\partial x} + v\frac{\partial v}{\partial y} + w\frac{\partial v}{\partial z} = -\frac{\partial p}{\partial y} + \frac{1}{R}\Big(\frac{\partial^2 v}{\partial x^2} + \frac{\partial^2 v}{\partial y^2} + \frac{\partial^2 v}{\partial z^2}\Big), \tag{2.7}$$

$$\frac{\partial w}{\partial t}+u\frac{\partial w}{\partial x}+v\frac{\partial w}{\partial y}+w\frac{\partial w}{\partial z}=-\frac{\partial p}{\partial z}+\frac{1}{R}\Big(\frac{\partial^2 w}{\partial x^2}+\frac{\partial^2 w}{\partial y^2}+\frac{\partial^2 w}{\partial z^2}\Big), \tag{2.8}$$

where R is the Reynolds number, defined as

$$R=\rho^*_\infty U^*_\infty \delta^*/\mu^*_\infty. \tag{2.9}$$

2.3. *Linearized perturbation equations*

Let $\bar{\mathbf{Q}}(x,y)$ denote the three-dimensional base flow field. When it is perturbed by a small-amplitude disturbance $\mathbf{Q}'(x,y,z,t)$, the total flow field $\mathbf{Q}(x,y,z,t)$ is written as

$$\begin{aligned}\mathbf{Q}=(u,v,w,p)=&\ \Big(\bar{u}(x,y),\bar{v}(x,y),\bar{w}(x,y),\bar{p}(x,y)\Big)+(u',v',w',p')\\ \equiv&\ \bar{\mathbf{Q}}(x,y)+\mathbf{Q}'(x,y,z,t).\end{aligned} \tag{2.10}$$

Substituting (2.10) into (2.5)-(2.8), and linearizing about the base flow, we obtain the linear N-S equations for the perturbation. For the ensuing analysis, it is convenient to cast them into the matrix form,

$$\Big[\tilde{\mathbf{A}}+\tilde{\mathbf{B}}_1\frac{\partial}{\partial x}+\tilde{\mathbf{B}}_2\frac{\partial}{\partial y}+\tilde{\mathbf{B}}_3\frac{\partial}{\partial z}+\tilde{\mathbf{C}}(-R\frac{\partial}{\partial t}+\frac{\partial^2}{\partial x^2}+\frac{\partial^2}{\partial y^2}+\frac{\partial^2}{\partial z^2})\Big]\mathbf{Q}'=\mathbf{0}, \tag{2.11}$$

where we have put

$$\tilde{\mathbf{A}}(x,y)=\begin{bmatrix}0&0&0&0\\ \partial\bar{u}/\partial x&\partial\bar{u}/\partial y&0&0\\ \partial\bar{v}/\partial x&\partial\bar{v}/\partial y&0&0\\ \partial\bar{w}/\partial x&\partial\bar{w}/\partial y&0&0\end{bmatrix},\quad \tilde{\mathbf{B}}_1(x,y)=\begin{bmatrix}1&0&0&0\\ \bar{u}&0&0&1\\ 0&\bar{u}&0&0\\ 0&0&\bar{u}&0\end{bmatrix}, \tag{2.12}$$

$$\tilde{\mathbf{B}}_2=\begin{bmatrix}0&1&0&0\\ \bar{v}&0&0&0\\ 0&\bar{v}&0&1\\ 0&0&\bar{v}&0\end{bmatrix},\ \tilde{\mathbf{B}}_3=\begin{bmatrix}0&0&1&0\\ \bar{w}&0&0&0\\ 0&\bar{w}&0&0\\ 0&0&\bar{w}&1\end{bmatrix},\ \tilde{\mathbf{C}}=-\frac{1}{R}\begin{bmatrix}0&0&0&0\\ 1&0&0&0\\ 0&1&0&0\\ 0&0&1&0\end{bmatrix}. \tag{2.13}$$

Since the base flow is steady and uniform in the spanwise direction, the perturbation $\mathbf{Q}'(x,y,z,t)$ can be written as

$$\mathbf{Q}'(x,y,z,t)=\phi(x,y)\exp[i(\beta z-\omega t)]+c.c., \tag{2.14}$$

where ω and β are real constants, but the shape function $\phi(x,y)$ depends on x and y. Substitution of (2.14) into (2.11) yields the equations governing ϕ,

$$\hat{\mathbf{A}}\phi+\hat{\mathbf{B}}\frac{\partial\phi}{\partial x}+\hat{\mathbf{C}}\frac{\partial^2\phi}{\partial x^2}=\mathbf{0}, \tag{2.15}$$

where

$$\phi(x,y)=\begin{bmatrix}\hat{u}\\ \hat{v}\\ \hat{w}\\ \hat{p}\end{bmatrix},\quad \hat{\mathbf{A}}(x,y)=\begin{bmatrix}0&D&i\beta&0\\ \partial\bar{u}/\partial x+s&\partial\bar{u}/\partial y&0&0\\ \partial\bar{v}/\partial x&\partial\bar{v}/\partial y+s&0&D\\ \partial\bar{w}/\partial x&\partial\bar{w}/\partial y&s&i\beta\end{bmatrix}, \tag{2.16}$$

$$\hat{\mathbf{B}}(x,y)=\begin{bmatrix}1&0&0&0\\ \bar{u}&0&0&1\\ 0&\bar{u}&0&0\\ 0&0&\bar{u}&0\end{bmatrix},\quad \hat{\mathbf{C}}=-\frac{1}{R}\begin{bmatrix}0&0&0&0\\ 1&0&0&0\\ 0&1&0&0\\ 0&0&1&0\end{bmatrix}, \tag{2.17}$$

with

$$s=\bar{v}D+i\beta\bar{w}-i\omega-[D^2+(i\beta)^2]/R,\quad D=\partial/\partial y. \tag{2.18}$$

Note that no assumption is made of the slow variation with x of either the base flow or the perturbation.

2.4. *Boundary conditions*

2.4.1. *Boundary conditions on the wall and at infinity*

The abrupt change is created through the boundary conditions at the wall. We consider first the case associated with an abrupt change of wall porosity: a finite section of porous plate joining two rigid sections. A general theory for the flow through a porous medium does not exist. We shall adopt the model based on the Darcy's law (Darcy 1856), which asserts that the velocity v^* is proportional to the pressure gradient driving the flow, namely,

$$v^* = -\frac{\kappa^*}{\mu^* b^*}(p_+^* - p_-^*), \tag{2.19}$$

where κ^* is the permeability of the medium, μ^* the dynamic viscosity of the fluid, b^* the thickness of the layer of the porous medium and $(p_+^* - p_-^*)$ represents the pressure difference across the medium. Typical intrinsic permeability κ^* ranges, in the unit of m^2, from 10^{-10} to 10^{-7} for pervious media, from 10^{-14} to 10^{-11} for semi-pervious media and from 10^{-19} to 10^{-15} for impervious media (http://en.wikipedia.org/wiki/Permeability_(fluid)).

The fluid motion may not respond to the pressure instantaneously as is implied in equation (2.19). A simple model that accounts for this inertial effect results from adding an extra term $\lambda_2^* \partial v^*/\partial t^*$ to (2.19) with λ_2^* being the relaxation time. When non-dimensionalized, the model for a porous wall reads

$$\lambda_2 \frac{\partial v}{\partial t} + v = -\lambda_1 p, \tag{2.20}$$

where we have set $p_-^* = 0$ without losing generality, and the dimensionless parameters

$$\lambda_1 = \frac{\kappa^*}{\mu^* b^*}\rho_\infty^* U_\infty^* = \frac{\kappa^*}{b^*} Re^*, \quad \lambda_2 = \lambda_2^* U_\infty/\delta^*. \tag{2.21}$$

For a unit Reynolds number $Re^* \approx 10^6 m^{-1}$ and a thickness $b^* \approx 10^{-2} m$, the range of λ_1 for pervious media is from 10^{-2} to 10. In spectral space, equation (2.20) can be written as $-i\omega\lambda_2\hat{v} + \hat{v} = -\lambda_1\hat{p}$, or

$$\hat{v} = -\lambda\hat{p} \quad \text{with} \quad \lambda = \frac{\lambda_1}{1 - i\omega\lambda_2}, \tag{2.22}$$

indicating that λ_2 can be absorbed into λ by allowing the latter to take complex values.

At the wall ($y = 0$), three boundary conditions are therefore imposed, namely,

$$\hat{u}(x,0) = \hat{w}(x,0) = 0, \quad \hat{v}(x,0) = \begin{cases} -\lambda\hat{p} & x_s < x < x_e, \\ 0 & \text{otherwise}, \end{cases} \tag{2.23}$$

where the first two correspond to the non-slip condition, and (x_s, x_e) indicates the extent of the porous panel.

For the case of a local steady suction, an inhomogeneous boundary condition is imposed on the steady transverse velocity (see later), but the unsteady perturbation satisfies homogeneous boundary conditions, $\hat{u} = \hat{w} = 0$ and $\hat{v} = 0$, with inhomogeneity appearing in the coefficients of its governing equations. The condition $\hat{v} = 0$ can be considered as corresponding to $\lambda_1(x) = \lambda_2(x) = 0$, and it follows that the boundary conditions are also given by equation (2.23) provided that we set $\lambda = 0$. Note that the suction of interest for

us is completely different from that considered in some previous studies (Pralits *et al.* 2002; Pralits & Hanifi 2003; Airiau *et al.* 2003), where the suction is imposed over the long length scale comparable with the distances to the leading edge, and its magnitude is of $O(R^{-1}U_\infty *)$. There the resulting steady flow is described by the classical boundary layer theory, and the instability waves developing on the slowly evolving base flow are described by PSE or LST. The local suction in the present paper occurs on a sufficiently short scale that both the steady base flow and unsteady disturbances exhibit full ellipticity. The aim of our work is to develop an approach that would supersede LST and PSE.

It should be stressed that while the oncoming instability wave is assumed to be of small amplitude, the sudden variations have not been assumed small at all. They either alter the base flow by $O(1)$ amount as in the case of a local suction, or produce an $O(1)$ abrupt change of the boundary conditions as in the cases of a finite porous panel and a rigid-porous junction. In either form, the rapid variation exerts an $O(1)$ influence on the amplitude of the oncoming instability wave.

At infinity, the perturbation vanishes, namely

$$(\hat{u}, \hat{v}, \hat{w}, \hat{p}) \to (0, 0, 0, 0) \quad \text{as} \quad y \to \infty. \tag{2.24}$$

2.4.2. *The upstream and downstream conditions: incident and transmitted waves*

In this paper, we will formulate LSA for abrupt isolated distortions neglecting the much weaker non-parallelism of the unperturbed base flow, an approximation consistent with that made in the high-Reynolds-number theory (Wu & Dong 2016) and justifiable by the latter.

In LSP, an incident wave is imposed upstream. For a localized scatter at x_c, the disturbance far upstream and downstream takes the form of a local eigen mode, that is,

$$\phi \to \tilde{\phi}(x, y) \exp\Big\{ i \int^x \alpha(x) dx \Big\} + c.c. \quad \text{as} \quad x - x_c \to \pm\infty, \tag{2.25}$$

where $\alpha(x)$ is the local streamwise wavenumber and $\tilde{\phi}(x, y)$ the corresponding eigenfunction. Under the local parallel-flow assumption, the streamwise variations of the base flow $\bar{\mathbf{Q}}$ and the eigenfunction $\tilde{\phi}$ are treated as being parametric. Then introducing (2.25) to (2.15) leads to

$$\mathbf{L}\,\tilde{\phi} \equiv \Big[\hat{\mathbf{A}} + i\alpha \hat{\mathbf{B}} + (i\alpha)^2 \hat{\mathbf{C}} \Big] \tilde{\phi} = \mathbf{0}, \tag{2.26}$$

which forms, along with the boundary conditions, an eigenvalue problem in LST.

The eigenvalue problem of LST for a parallel flow can be solved for a given ω at locations far upstream ($x - x_c \to -\infty$) and downstream ($x - x_c \to +\infty$) of x_c. The upstream condition is written as

$$\phi \to \phi_I = A_0 \tilde{\phi}_I(x, y) \exp\Big\{ i \int_{x_0}^x \alpha_I(x) dx \Big\} \quad \text{as} \quad x - x_c \to -\infty, \tag{2.27}$$

where α_I and $\tilde{\phi}_I$ denote the wavenumber and eigenfunction of the incident wave, respectively, and A_0 is the amplitude at a reference location $x_0 \ll x_c$ (and can be set to unity without losing generality). Similarly, the far downstream condition is (see figure 2)

$$\phi \to \phi_T = A_T \tilde{\phi}_T(x, y) \exp\Big\{ i \int_{x_c}^x \alpha_T(x) dx \Big\} \quad \text{as} \quad x - x_c \to +\infty, \tag{2.28}$$

in which the wavenumber α_T of the transmitted wave can be obtained by solving the local eigenvalue problem, but its amplitude A_T and eigenfunction $\tilde{\phi}_T$ are to be computed as part of the solution to the LSP.

For an isolated distortion and with the non-parallelism of the unperturbed base flow being neglected, the steady flows far upstream and downstream of the distortion are the same, and thus the incident instability mode and the transmitted wave have the same wavenumber and shape, that is,

$$\alpha_T(x) = \alpha_I(x) \equiv \alpha^{(0)}, \quad \tilde{\phi}_T(x,y) = \tilde{\phi}_I(x,y) \equiv \tilde{\phi}^{(0)}(y), \tag{2.29}$$

where $\alpha^{(0)}$ and $\tilde{\phi}^{(0)}(y)$ denote the eigenvalue and eigenfunction of the unperturbed base flow $\bar{\mathbf{Q}}(y)$.

When the non-parallelism of base flow is taken into account, (2.29) does not hold on. Nevertheless, a relation may be established between $\tilde{\phi}_I$ and $\tilde{\phi}_T$ by supposing that the porous plate and/or the downstream base flow is established from a rigid plate and/or the upstream base flow through a gradual variation of the porosity and the base state. Based on this idea, we show in the appendix that a matrix $\mathbf{T}$ can be introduced such that

$$\tilde{\phi}_T = \mathbf{T}\tilde{\phi}_I. \tag{2.30}$$

Since $\mathbf{T}$ links the eigenvector of the transmitted wave to that of the incident wave, it will be referred to as a transfer matrix. The details of its calculation is given in the appendix.

It follows from (2.2)-(2.3) and (2.29) that

$$A_T = TrA_0 \exp\{i\alpha^{(0)}(x_c - x_0)\},$$

and the upstream and downstream conditions, (2.27) and (2.28), can be rewritten as

$$\phi \to \quad \phi_I = A_0\tilde{\phi}^{(0)}(y)\exp\Big[i\alpha^{(0)}(x-x_0)\Big] \quad \text{as} \quad x - x_c \to -\infty, \tag{2.31}$$

$$\phi \to \phi_T = TrA_0\tilde{\phi}^{(0)}(y)\exp\Big[i\alpha^{(0)}(x-x_0)\Big] \quad \text{as} \quad x - x_c \to +\infty, \tag{2.32}$$

which imply that the upstream and downstream conditions are related to each other (see below).

In summary, the LSP is described by the boundary-value problem consisting of the partial differential equations (2.15), the boundary conditions (2.23)-(2.24) as well as the upstream and downstream conditions (2.31)-(2.32). This problem can be solved with the input of ω and $\alpha^{(0)}$ only without the need of specifying $\tilde{\phi}^{(0)}(y)$. Treated this way, the formulation poses an eigenvalue problem, in which the transmission coefficient Tr appears as the eigenvalue, and $\tilde{\phi}^{(0)}(y)$ is to be obtained as the far-field asymptote of $\phi(x,y)$, a fact that will transpire when the system is discretized.

2.5. *Disturbance characteristics*

In the presence of a scatter, the disturbance in its vicinity may be rather complex. Nevertheless, for a given disturbance quality $\phi(x,y)$, it is useful for interpretation and diagnostic purpose to define its local amplitude $A(x)$ and phase $\theta(x)$ at each location x as

$$A(x) = \max_y |\phi(x,y)|, \quad \theta(x) = \arg\Big(\phi(x,y_s)\Big), \tag{2.33}$$

where y_s denotes the position at which $|\phi|$ attains its maximum. Using $A(x)$ and $\theta(x)$, we can define the local growth rate $G(x)$ and wavenumber $K(x)$ as

$$G(x) = \frac{d\ln A(x)}{dx}, \quad K(x) = \frac{d\theta(x)}{dx}. \tag{2.34}$$

Far away from the scatter, the perturbation is an instability mode and so it is expected that

$$G \to -\alpha_i^{(0)}, \quad K \to \alpha_r^{(0)} \quad \text{as} \quad x - x_c \to \pm\infty, \tag{2.35}$$

where $\alpha^{(0)} = \alpha_r^{(0)} + i\alpha_i^{(0)}$ is the local wavenumber obtained by LST.

3. Numerical method

The general formulation presented in the previous section is now specialized to T-S instability waves in the Blasius boundary layer. The boundary-value problem governing the LSP is to be discretized and solved in the computational domain $[x_0, x_n] \times [0, y_J]$. In the streamwise direction, the domain $[x_0, x_n]$ is discretized into n intervals by $n+1$ mesh points x_i with $i \in [0, n]$. The value of a variable at a mesh point x_i will be indicated by the subscript i. The derivatives of ϕ in (2.15) with respect to x are approximated by using a series of five-point finite-difference schemes with fourth-order accuracy, namely

$$\frac{\partial \phi_i}{\partial x} \approx \sum_{l=-2}^{2} a_{i,l}\phi_{i+l}, \quad \frac{\partial^2 \phi_i}{\partial x^2} \approx \sum_{l=-2}^{2} b_{i,l}\phi_{i+l}, \tag{3.1}$$

where $a_{i,l}$ and $b_{i,l}$ are the approximation coefficients.

After replacing the partial derivatives with respect to x by the corresponding finite-difference approximations, equation (2.15) can be rewritten as

$$\mathbf{A}_i\phi_{i-2} + \mathbf{B}_i\phi_{i-1} + \mathbf{C}_i\phi_i + \mathbf{D}_i\phi_{i+1} + \mathbf{E}_i\phi_{i+2} = \mathbf{0}, \tag{3.2}$$

where we have put

$$\begin{cases} \mathbf{A}_i = b_{i,-2}\hat{\mathbf{C}}_i + a_{i,-2}\hat{\mathbf{B}}_i, \\ \mathbf{B}_i = b_{i,-1}\hat{\mathbf{C}}_i + a_{i,-1}\hat{\mathbf{B}}_i, \\ \mathbf{C}_i = b_{i,0}\hat{\mathbf{C}}_i + a_{i,0}\hat{\mathbf{B}}_i + \hat{\mathbf{A}}_i, \\ \mathbf{D}_i = b_{i,1}\hat{\mathbf{C}}_i + a_{i,1}\hat{\mathbf{B}}_i, \\ \mathbf{E}_i = b_{i,2}\hat{\mathbf{C}}_i + a_{i,2}\hat{\mathbf{B}}_i. \end{cases} \tag{3.3}$$

The operator $D = \partial/\partial y$ in (2.15) can be discretized by a fourth-order Malik scheme (Malik 1990) taking into account the boundary conditions (2.23)-(2.24). The absence of a boundary condition for $\hat{p}$ at the wall is, as usual, remedied by discretizing the normal pressure gradient, $\partial\hat{p}/\partial y$, on a staggered grid, i.e. at the centre of each interval between two adjacent mesh points.

The mesh in the x-direction is uniform with grid points $x_i = x_0 + i\Delta x$ $(0 \leqslant i \leqslant n)$, where $\Delta x = (x_n - x_0)/n$. In the y-direction, a non-uniform mesh is used with its size being gradually stretched with the distance according to

$$y_j = y_J \frac{4\eta}{4 + (\sqrt{1+8k_1} - 3)(1-\eta^2)}, \quad \eta = \frac{j}{J} - \frac{k_2 - 1}{\pi(k_2+1)}\sin(\pi\frac{j}{J}) \quad (0 \leqslant j \leqslant J), \tag{3.4}$$

where k_1 and k_2 are constants controlling the stretching since $\Delta y_J/\Delta y_0 = k_1 \times k_2$. The default parameters are selected as $y_J = 100$, $k_1 = 100$, $k_2 = 60$ and $J = 200$.

At the inlet x_0, which we take as the reference location, the perturbation is of the form,

$$\phi_0 = A_0\tilde{\phi}^{(0)}, \tag{3.5}$$

as indicated by (2.31), from which it also follows that for $x_{-1} = x_0 - \Delta x$ and $x_{-2} = x_0 - 2\Delta x$,

$$\phi_{-1} = \phi_0 \exp\Big[-i\alpha^{(0)}\Delta x\Big], \quad \phi_{-2} = \phi_0 \exp\Big[-2i\alpha^{(0)}\Delta x\Big]. \tag{3.6}$$

Inserting (3.6) into (3.2) for $i = 0$ and $i = 1$ yields

$$\check{\mathbf{C}}_0\phi_0 + \mathbf{D}_1\phi_1 + \mathbf{E}_1\phi_2 = \mathbf{0}, \tag{3.7}$$

$$\check{\mathbf{B}}_1\phi_0 + \mathbf{C}_1\phi_1 + \mathbf{D}_1\phi_2 + \mathbf{E}_1\phi_3 = \mathbf{0}, \tag{3.8}$$

where

$$\begin{cases} \check{\mathbf{C}}_0 = \mathbf{C}_0 + \mathbf{B}_0 \exp\left[-i\alpha^{(0)}\Delta x\right] + \mathbf{A}_0 \exp\left[-2i\alpha^{(0)}\Delta x\right], \\ \check{\mathbf{B}}_1 = \mathbf{B}_1 + \mathbf{A}_1 \exp\left[-i\alpha^{(0)}\Delta x\right]. \end{cases} \tag{3.9}$$

Similarly, the perturbation at the outlet $x = x_n$, representing the transmitted instability wave, can be written as

$$\phi_n = TrA_0\tilde{\phi}^{(0)}(y) \exp\left[i\alpha^{(0)}(x_n - x_0)\right] \tag{3.10}$$

according to (2.32), which also implies that the perturbation in the vicinity of the outlet can be expressed as

$$\phi(x, y) = \phi_n \exp\left[i\alpha^{(0)}(x - x_n)\right], \tag{3.11}$$

and specifically for $x_{n+1} = x_n + \Delta x$ and $x_{n+2} = x_n + 2\Delta x$,

$$\phi_{n+1} = \phi_n \exp\left[i\alpha^{(0)}\Delta x\right], \quad \phi_{n+2} = \phi_n \exp\left[2i\alpha^{(0)}\Delta x\right]. \tag{3.12}$$

On the other hand, it follows from (3.5) and(3.10) that the perturbations at the inlet and outlet are related via the equation

$$\phi_n = Tr\phi_0 \exp\left[i\alpha^{(0)}(x_n - x_0)\right]. \tag{3.13}$$

Inserting (3.12) into (3.2) for $i = n - 1$ and $i = n$, and making use of (3.13), we obtain the relations,

$$\mathbf{A}_{n-1}\phi_{n-3} + \mathbf{B}_{n-1}\phi_{n-2} + \mathbf{C}_{n-1}\phi_{n-1} = Tr\check{\mathbf{E}}_{n-1}\phi_0, \tag{3.14}$$

$$\phi_n = Tr\check{\mathbf{D}}_n\phi_0, \tag{3.15}$$

which describe the behaviour of the disturbance near the outlet, where we have put

$$\check{\mathbf{E}}_{n-1} = -\left\{\mathbf{D}_{n-1} + \mathbf{E}_{n-1} \exp\left[i\alpha^{(0)}\Delta x\right]\right\} \exp\left[i\alpha^{(0)}(x_n - x_0)\right], \tag{3.16}$$

$$\check{\mathbf{D}}_n = \mathbf{I} \exp\left[i\alpha^{(0)}(x_n - x_0)\right]. \tag{3.17}$$

When the non-parallelism of base flow is taken into account, a transfer matrix $\mathbf{T}$ will appear in (3.16) and (3.17), and the eigenvalue $\alpha^{(0)}$ will be replaced by α_I at inlet and α_T at outlet, respectively.

The system of the linear algebraic equations, consisting of the inlet conditions (3.7)-(3.8), the outlet conditions (3.14)-(3.15) and the equations at interior points, (3.2), can

be written in the matrix form as

$$\begin{bmatrix} \check{\mathbf{C}}_0 & \mathbf{D}_0 & \mathbf{E}_0 & \mathbf{0} & \mathbf{0} \\ \check{\mathbf{B}}_1 & \mathbf{C}_1 & \mathbf{D}_1 & \mathbf{E}_1 & \mathbf{0} \\ \mathbf{A}_i & \mathbf{B}_i & \mathbf{C}_i & \mathbf{D}_i & \mathbf{E}_i \\ \mathbf{0} & \mathbf{A}_{n-1} & \mathbf{B}_{n-1} & \mathbf{C}_{n-1} & \mathbf{0} \\ \mathbf{0} & \mathbf{0} & \mathbf{0} & \mathbf{0} & \mathbf{I} \end{bmatrix} \begin{Bmatrix} \phi_0 \\ \phi_1 \\ \phi_i \\ \phi_{n-1} \\ \phi_n \end{Bmatrix} = Tr \begin{bmatrix} \mathbf{0} & \mathbf{0} & \mathbf{0} & \mathbf{0} & \mathbf{0} \\ \mathbf{0} & \mathbf{0} & \mathbf{0} & \mathbf{0} & \mathbf{0} \\ \mathbf{0} & \mathbf{0} & \mathbf{0} & \mathbf{0} & \mathbf{0} \\ \check{\mathbf{E}}_{n-1} & \mathbf{0} & \mathbf{0} & \mathbf{0} & \mathbf{0} \\ \check{\mathbf{D}}_n & \mathbf{0} & \mathbf{0} & \mathbf{0} & \mathbf{0} \end{bmatrix} \begin{Bmatrix} \phi_0 \\ \phi_1 \\ \phi_i \\ \phi_{n-1} \\ \phi_n \end{Bmatrix}, \quad (3.18)$$

which poses a generalized eigenvalue problem with Tr being the eigenvalue and $(\phi_0, \phi_1, \phi_i, \phi_{n-1}, \phi_n)^T$ the eigenvector. The matrix in the eigenvalue problem (3.18) is much larger than that of LST. Fortunately, since the coefficient matrix is block pentadiagonal, the system (3.18) can be reduced first, at little computation cost by using the block Gaussian elimination with partial or complete pivoting, to

$$\begin{bmatrix} \mathbf{I} & \mathbf{0} & \mathbf{0} & \mathbf{0} & \mathbf{0} \\ \breve{\mathbf{B}}_1 & \mathbf{I} & \mathbf{0} & \mathbf{0} & \mathbf{0} \\ \breve{\mathbf{A}}_i & \breve{\mathbf{B}}_i & \mathbf{I} & \mathbf{0} & \mathbf{0} \\ \mathbf{0} & \breve{\mathbf{A}}_{n-1} & \breve{\mathbf{B}}_{n-1} & \mathbf{I} & \mathbf{0} \\ \mathbf{0} & \mathbf{0} & \breve{\mathbf{A}}_n & \breve{\mathbf{B}}_n & \mathbf{I} \end{bmatrix} \begin{Bmatrix} \phi_0 \\ \phi_1 \\ \phi_i \\ \phi_{n-1} \\ \phi_n \end{Bmatrix} = Tr \begin{bmatrix} \breve{\mathbf{E}}_0 & \mathbf{0} & \mathbf{0} & \mathbf{0} & \mathbf{0} \\ \breve{\mathbf{E}}_1 & \mathbf{0} & \mathbf{0} & \mathbf{0} & \mathbf{0} \\ \breve{\mathbf{E}}_i & \mathbf{0} & \mathbf{0} & \mathbf{0} & \mathbf{0} \\ \breve{\mathbf{E}}_{n-1} & \mathbf{0} & \mathbf{0} & \mathbf{0} & \mathbf{0} \\ \breve{\mathbf{D}}_n & \mathbf{0} & \mathbf{0} & \mathbf{0} & \mathbf{0} \end{bmatrix} \begin{Bmatrix} \phi_0 \\ \phi_1 \\ \phi_i \\ \phi_{n-1} \\ \phi_n \end{Bmatrix}, \quad (3.19)$$

which in turn reduces farther to

$$\Big[\mathbf{I} + Tr\breve{\mathbf{E}}_0\Big]\phi_0 = \mathbf{0}, \quad (3.20)$$

where Tr is the eigenvalue and ϕ_0 the eigenvector. Obviously, the amount of computation to solve the eigenvalue problem (3.20) is comparable with that for solving LST, and so is the computation cost of solving the original eigenvalue problem (3.18) since the operation count of the block Gaussian elimination is a small fraction of the overall calculation. As alluded to earlier, the eigenfunction of the incident and transmitted waves is calculated rather than being imposed.

The influence of a local change on transition has also been studied by performing a local stability analysis for the distorted mean flow and/or modified boundary conditions. This amounts to assuming that the perturbation in the whole domain is of a normal-mode form, which is not true when the local change takes place over a length scale comparable with, or smaller than, the wavelength of the instability. In order to assess the validity of that approach, we also solve the local stability problem at each $x_i \in [x_0, x_n]$. Let $\alpha_s(x)$ and $\alpha(x)$ denote the local wavenumber in the presence and absence of the scatter respectively. Then the amplitude evolves according to

$$A_{LST}(x) = A_0 \exp\Big\{i\int_{x_0}^{x} \alpha_s(x)dx\Big\}. \quad (3.21)$$

It follows that the transmission coefficient can be expressed as

$$Tr = \exp\Big\{i\int_{x_0}^{x_n} \Big[\alpha_s(x) - \alpha(x)\Big]dx\Big\}. \quad (3.22)$$

The LST predictions, (3.21) and (3.22), will be referred to as LST, and comparisons with LSA will be made.

Compared with LST, PSE and DNS, the advantages of LSA are as follows. (i) The disturbance is governed by the linearized N-S equations without making the local parallel-flow approximation of the distorted flow in LST or parabolization in PSE. As a result, the solution can describe the rapid change in the streamwise direction, which is not possible with either LST or PSE. On the other hand, LSA remains valid wherever LST or PSE

is applicable. (ii) The inlet and outlet boundary conditions are specified properly and easily, whereas it is rather problematic to impose initial boundary conditions in PSE and inlet/outlet boundary conditions in DNS. (iii) The linear algebraic equations can be solved by block Gaussian elimination with the time and complexity involved being equivalent to those in PSE and LST. Due to the frequency-domain formulation and linearization, the algebraic system and computational time are much reduced compared with usual DNS in time domain. LSA provides a new and appropriate perspective to study and quantify the effect of an abrupt change on instability and transition. The transmission coefficient describes the overall effect of the scatter. While the behavior of the disturbance near the scatter can be studied in detail using LSA, it is, in many practical applications, of less a concern than the relationship between the incident and transmitted waves. In such cases, it is useful to compute and document the transmission coefficients systematically for various parameters characterizing the scatter. The resulting data can be used with LST or PSE methods, which remain applicable in the regions far up- and down-stream of the scatter, to predict the global evolution of the disturbance. By using the transmission coefficient, the traditional e^N-method may be extended to correlate transition in the presence of sudden variations, namely, if transition is deemed to occur where $N = N_c$ in the smooth case, the criterion then becomes $N = N_c - \ln|Tr|$ when a single scatter is present, or more generally

$$N = N_c - \sum_k \ln|Tr_k|, \tag{3.23}$$

when multiple well-separated scatters are present, where Tr_k denotes the transmission coefficient of each scatter.

4. Numerical results

The unperturbed base flow is taken to be the Blasius boundary layer over a flat plate. With its non-parallelism being neglected, the local profile at x_c^*, the centre of the porous panel or suction slot, is used. The reference length δ^* is taken to be the displacement thickness of the Blasius boundary layer at x_c^*.

In order to make the results more accessible to a general reader, the familiar non-dimensional frequency $F \equiv \omega^*\nu/U_\infty^{*2} \times 10^6$, which is independent of the reference length, will be used. It is related to ω via

$$F = \omega/R \times 10^6. \tag{4.1}$$

4.1. *Local porous wall*

Calculations were first carried out for a local porous panel. The dynamics of the panel is described by (2.22), in which λ takes complex values, $\lambda(x) = \lambda_m e^{i\varphi} f(x)$, with $\varphi \in (-\pi/2, 0]$ being the phase difference between the velocity and pressure fluctuations, and the distribution of the porosity is taken to be

$$f(x) = \Big\{\tanh[(x - x_c + d/2)/\Delta] - \tanh[(x - x_c - d/2)/\Delta]\Big\}/2, \tag{4.2}$$

where x_c denotes the centre of the panel and d is a measure of its width, whilst Δ is the length scale in which the wall changes from being rigid to porous and vice versa. We take $\Delta \ll d$ so that the distribution is of top-hat form, featuring an almost constant non-zero porosity λ_m over a length d, beyond which the wall is practically rigid. Therefore d and Δ will be referred to as panel width and junction width respectively.

In order to validate the theoretical formulation and prediction of LSA, a DNS in time

domain and involving a sponge zone has been performed. The method and the code were developed by Huang *et al.* (2005*b*). The convective terms are split and approximated by a fifth-order weak upwind difference scheme while the viscous terms are discretized by applying twice an eighth-order central difference scheme for the first-order derivative. The scheme for the viscous terms is suboptimal in comparison with a direct approximation of the second-order derivative because it looses in accuracy for a given grid size (Babucke *et al.* 2008). However, it is sufficiently accurate in our calculations since we used a fine resolution with 180 mesh points in one wavelength. The governing equations are integrated fully explicitly in time by using a third-order TVD Runge-Kutta method. As the base flow, the Blasius similarity solution at x_c is not a stationary solution of the N-S equations, a suitable small steady source term of $O(10^{-6})$ is added to the N-S equations (Huang *et al.* 2005*a*) in order to render this local Blasius solution a steady state. Furthermore, the boundary condition on the porous wall, (2.20), is changed to

$$\lambda_2 \frac{\partial(v-\bar{v})}{\partial t} + (v-\bar{v}) = -\lambda_1(p-\bar{p}), \tag{4.3}$$

where $\bar{v}$ and $\bar{p}$ are the normal velocity and pressure of the base flow respectively. This ensures that porosity affects only the unsteady perturbation as it does in our theoretical modelling.

The DNS is conducted for a finite porous wall centred at x_c, where the local Reynolds number $R_c = 1262$. The porosity adjustment is described by $\lambda_1 = \lambda_m f(x)$ and $\lambda_2 = 0$ with $\lambda_m = 2$ and $f(x)$ being given by (4.2), in which $d = 27$ and $\Delta = 0.8$, 3.2. The relatively large λ_m and small Δ signify an abrupt change of porosity, which presents a computational challenge as a fine resolution in the streamwise direction is required. The computational domain covers the Reynolds number range $1000 < R < 1577$. A T-S wave with a frequency $F = 60$, for which the corresponding wavelength $\lambda_{TS} = 27$, is imposed at the inlet. A very small amplitude $A_0 = 10^{-6}$ is specified to ensure that the perturbation remains essentially linear in the entire region of interest. A mesh size $\Delta x = 0.15$ is used, for which there are 180 points within one wavelength. The number of points in the wall-normal direction is 201, resulting in more than 120 points in one boundary-layer thickness and the mesh size Δy at the wall being smaller than 0.002. The time step is $\Delta t = 2.5 \times 10^{-5}$, giving rise to a Courant-Friedrichs-Lewy (CFL) number of 0.25. Calculations using smaller Δt and Δy were found to give the same result.

Figures 3 (a-1) and (a-2) show the evolution of the amplitude obtained by three different methods: DNS, LSA and LST for $\Delta = 0.8$ and 3.2, respectively. The corresponding local amplification rates G are displayed in (b-1) and (b-2). The predictions by LSA and DNS agree quite well, and especially both capture the fine detail of the adjustment, which is sharper for smaller Δ (corresponding to a more abrupt change). For smaller Δ, the amplitude exhibits double peaks. The dash-dotted lines, labelled as 'rigid, E.F.' in figures 3 (a-1) and (a-2) represent the forward extrapolation of the otherwise continued exponential growth of the oncoming mode if the wall were rigid, and as is indicated by the dashed lines labelled as 'rigid, E.B.', the eventual modal growth far downstream is also extrapolated backward using the growth rate for the rigid wall. From these, the transmission coefficient is found to be 6.39 and 7.61 for $\Delta = 0.8$ and 3.2 respectively, exact the same as what LSA predicts directly. In the upstream and downstream limits, the amplitude matches smoothly with the exponential growth. The formulation and prediction of LSA are therefore validated. The amplitude obtained by LST (see (3.21)) is however significantly below that by LSA, and most notably LST fails completely to capture the non-monotonic behavior of the amplitude. The modifications to the local wavelength are shown in (c-1) and (c-2). The violent 'step-like' behaviour of G and K

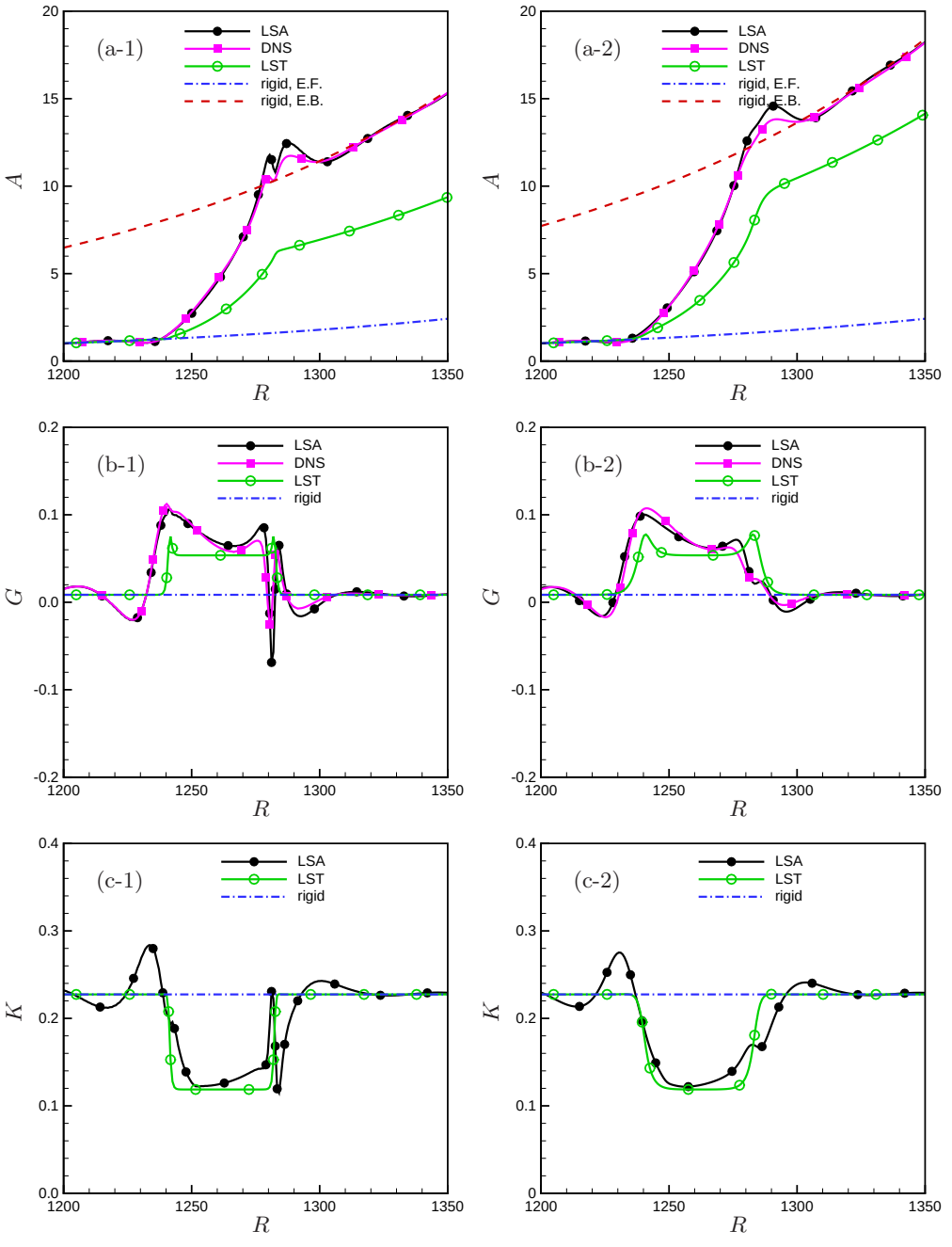

FIGURE 3. The local amplitude A, growth rate G and the wavenumber K versus the local Reynolds number R for the case of a T-S wave with frequency $F = 60$ scattered by a local porous panel centred at $R_c = 1262$ with $d = 27$, $\lambda_m = 2$ and $\varphi = 0^\circ$. The figures (a-1)-(c-1) on the left-hand side are for $\Delta = 0.8$, and the figures (a-2)-(c-2) on the right-hand side are for $\Delta = 3.2$. The dash-dotted lines (labelled as 'rigid, E.F.') represent the continued exponential growth of the incident T-S wave if the wall were rigid, whereas the dashed lines (labelled as 'rigid, E.B.') represent the backward extrapolation of the transmitted wave using the growth rate for the flat rigid wall.

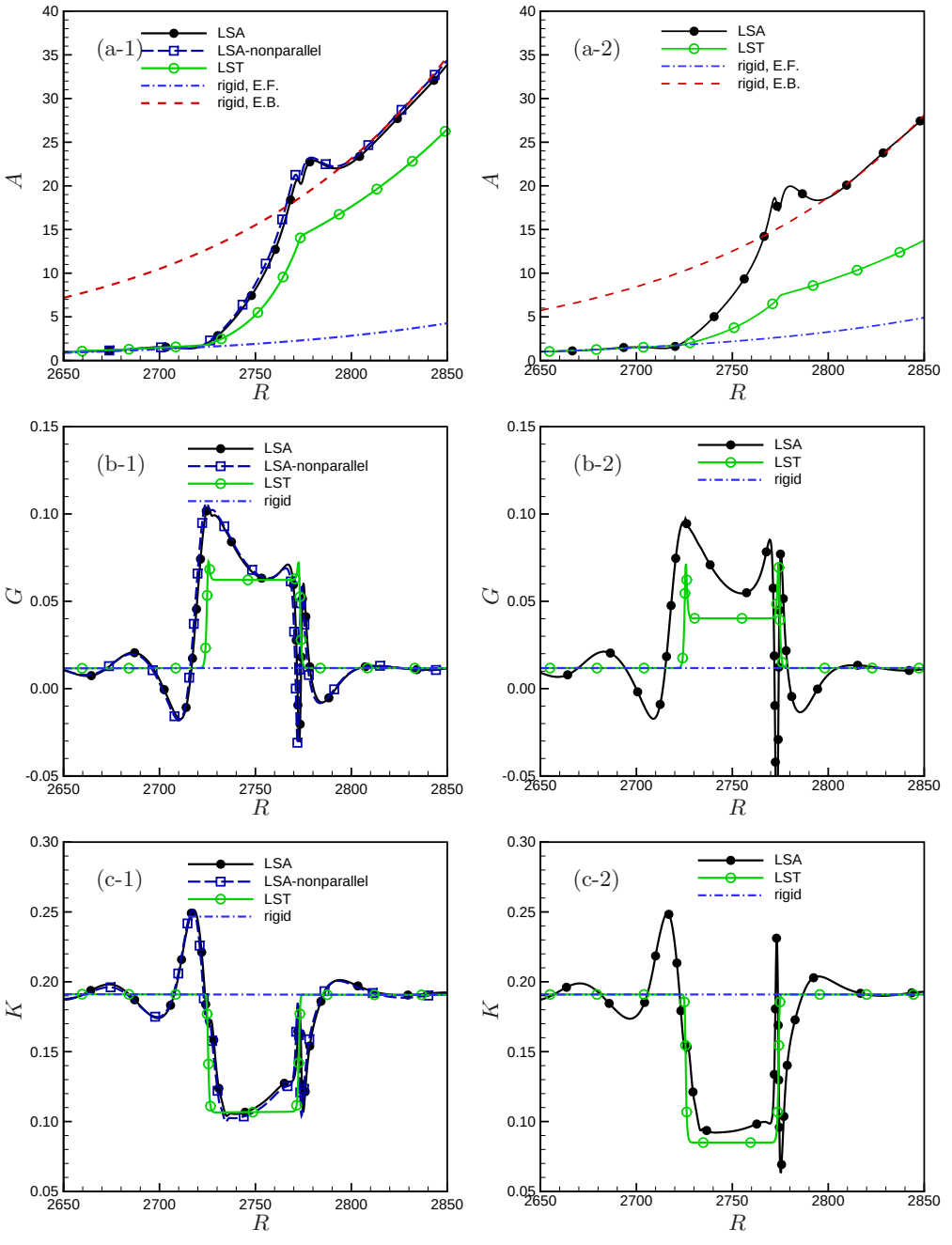

FIGURE 4. The local amplitude A, growth rate G and wavenumber K versus the local Reynolds number R for the case of a T-S wave with frequency $F = 20$ scattered by a local porous panel centred at $R_c = 2750$ with $d = 32$, $\Delta = 0.73$ and $\varphi = 0^\circ$. The figures (a-1)-(c-1) on the left-hand side are for $\lambda_m = 1$, and the figures (a-2)-(c-2) on the right-hand side are for $\lambda_m = 2$. The dash-dotted lines (labelled as 'rigid, E.F.') represent the continued exponential growth of the incident T-S wave when the wall were rigid, while the dashed lines (labelled as 'rigid, E.B.') represent the backward extrapolation of the transmitted wave using the growth rate for the flat rigid wall.

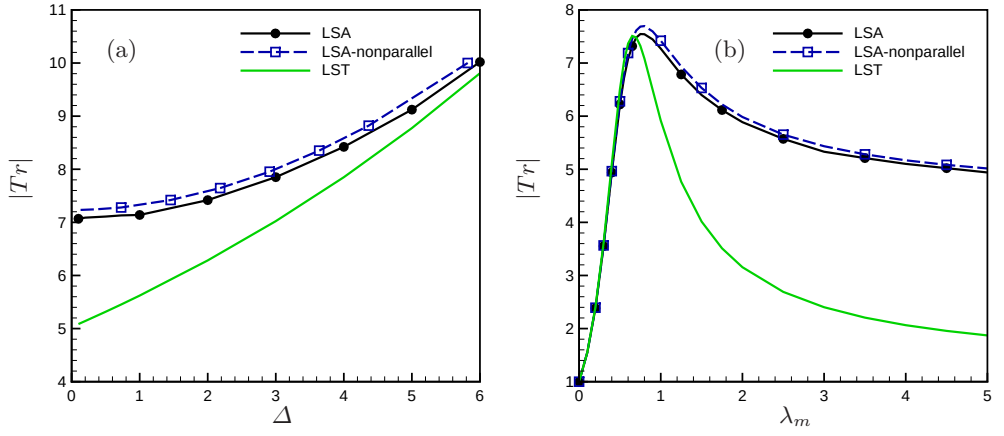

FIGURE 5. Effects of the junction width Δ and porosity λ_m on the transmission coefficient Tr for a T-S wave with $F = 20$ interacting with a finite local porous panel centred at $R_c = 2750$ with $d = 32$ and $\varphi = 0°$: (a) Tr versus Δ with $\lambda_m = 1$; (b) Tr versus λ_m with $\Delta = 1.46$.

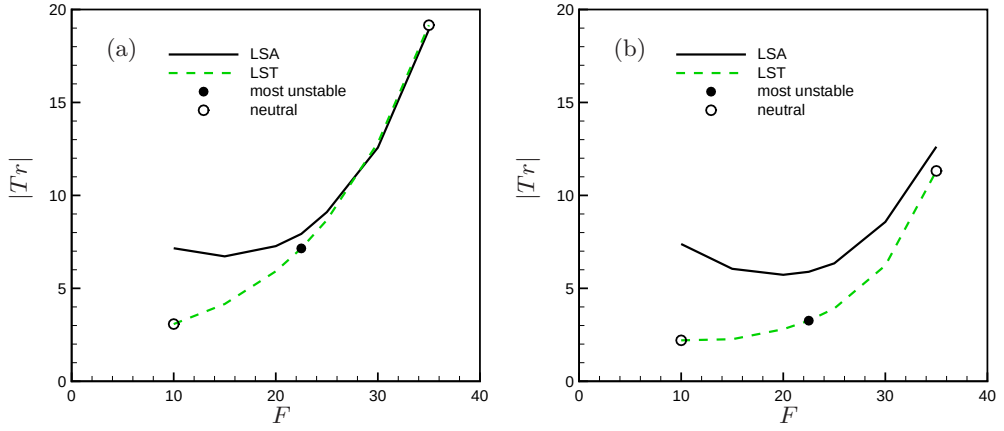

FIGURE 6. Variation of the transmission coefficient Tr with the wave frequency F for a local porous panel centered at $R_c = 2750$ with $d = 32$, $\varphi = 0°$: (a) $\Delta = 1.46$, $\lambda_m = 1$; (b) $\Delta = 0.73$, $\lambda_m = 2$. Symbols: ○, frequency of the neutral mode; ●, frequency of the most unstable mode.

highlights the strong non-parallelism, which cannot be accounted for by LST or PSE. It is worth mentioning that the simulation on a 256-core parallel cluster takes 40 hours to reach a statistically steady state, whereas LSA requires only about a few minutes on one core and is therefore much more efficient. The LST solution can be obtained in one minute on one core, but its validity is restricted to relatively small λ_m and large Δ as will be shown later. Among the three methods, LSA is accurate and most efficient.

Figure 4 displays the results for the case of a T-S wave with frequency $F = 20$ scattered by a porous panel centred at $R_c = 2750$ with $d = 32$, $\Delta = 0.73$ and $\varphi = 0°$. Here the value of d corresponds to approximately one wavelength of the imposed T-S wave. Two different porosities, $\lambda_m = 1$ and 2, are considered. For the former value, the prediction considering the non-parallelism is re-plotted (labelled as 'LSA-nonparallel'). The comparison indicates that the amplitude evolution, the local growth rate and wavenumber of the disturbance exhibit little difference with or without accounting for the non-parallelism of the base flow, indicating that the effect of non-parallelism of base

flow is much weaker than that of the abrupt changes. The computational domain covers the Reynolds number range $2000 < R < 3334$, larger than what is shown in figure 4. LST indicates that the boundary layer over a porous surface is considerably more unstable. This is reminiscent of ultrasonically absorptive coating (UAC), which is known to destabilize first modes (but stabilize second Mack modes) on supersonic boundary layers. The destabilizing effects in the two cases are consistent since first modes are continuation of T-S waves into the supersonic regime, and UAC may be modelled by a model similar to that for a porous wall (Fedorov 2011). The predictions of LSA are compared with those by usual LST. The amplitude, local growth rate and wavenumber for the porosity $\lambda_m = 1$ with a small junction width (i.e. sharp change) are displayed in figures 4(a-1, b-1, c-1). There is a sharp increase of the amplitude in the region over the scatter, and consequently the amplitude downstream is much higher than that attained without the porous panel. The transmission coefficient $Tr \approx 7$, significantly greater than unity. It is interesting to note that the amplitude predicted by LSA varies over a length that is several times of the panel width d with the effect of the porous panel extending to both the upstream and downstream directions. The upstream influence is expected because of the elliptic nature of the LSA formulation. Most strikingly, the evolution is non-monotonic. LST also captures the enhanced amplification as is indicated in figure 4(a-1). However, the predicted amplitude evolution is monotonic rather than oscillatory, and the predicted variation is confined within the porous section. This is because in the LST formulation, the effect of porosity is completely local, exerted through the boundary condition. The LSA results in Figure 4(b-1) indicate that the porous effect is destabilizing overall, causing the local growth rate to increase by a factor of 6 at the center of the local porous panel, but near the junctions there is a local stabilizing effect and this leads to the non-monotonic behaviour of A. The local porous wall also changes the wavenumber appreciably as is indicated in figure 4(c-1). LST predicts the overall features of enhanced growth rate and wavenumber variation, but fails to capture the upstream influence and detailed characteristics, especially those near the junctions. Unlike LSA, LST predicts that a porous wall is uniformly destabilizing. Figures 4(a-2, b-2, c-2) show the results for a larger porosity, $\lambda_m = 2$. The overall features are similar to those for $\lambda_m = 1$, except that the variations of the amplitude, growth rate and wavenumber near the second junction region become sharper. Furthermore, the differences between the predictions by LSA and LST become larger, suggesting that LST would give even worse predictions when the porosity λ_m is increased further.

Figure 5 shows the effects of the junction width Δ and the porosity λ_m on the transmission coefficient Tr. As figure 5(a) indicates, Tr increases monotonically with Δ. For a finite Δ, the transmission coefficient Tr predicted by LSA consists of both the distributed effect of the enhanced local growth rate in the porous region and the local effect of the junctions, but the Tr given by LST (see (3.22)) accounts for, in a rather approximate manner, the former effect only. The two are therefore different. The difference is the largest in the limit $\Delta \to 0$ with the discrepancy of 2.2 representing the pure effect of sharp junctions. As Δ increases, the difference between the LSA and LST predictions becomes smaller because the distributed effect dominates whilst the pure junction effect weakens. Figure 5(b) shows that the Tr predicted by LSA first increases with λ_m, reaching a maximum at $\lambda_m \approx 1$, after which Tr decreases but still maintains at a value significantly greater than unity. LST captures the same trend, and in particular for $0 \leqslant \lambda_m \leqslant 1$, the prediction by LST is in agreement with that by LSA. However, significant deviation arises for $\lambda_m > 1$ with the transmission coefficient predicted by LST being just a fraction of that given by LSA. The base-flow non-parallelism is found to make a negligible difference of less than 3%, and its minor role in the scattering

process is reaffirmed. The cause of scattering is the strong inhomogeneity associated with the short-scale change of the porosity.

We also investigated the variation of the transmission coefficient with the frequency, and the results are shown in figure 6 for $\Delta = 1.46$ and 0.73. As is indicated, LSA predicts that as the frequency increases from that of the neutral mode, the transmission coefficient $|Tr|$ first decreases slightly and then increases rather steeply with F. In contrast, LST predicts a monotonic increase with F. The LST prediction for relatively small F is of course erroneous, but approaches the correct value given by LSA for large F. The latter is expected since T-S modes of higher frequency have wavelengthes shorter than the length scale of the mean-flow distortion, and so LST eventually becomes applicable. The result that higher-frequency T-S waves are more sensitive to the destabilization is of interest. An analytical treatment may be taken to obtain the asymptotic behaviour of Tr in the high-frequency limit, but the pursuit of this line is beyond the scope of this paper.

4.2. *Local steady suction*

We now consider scattering of a T-S wave by the mean-flow distortion induced by a local steady suction. The calculations were carried out for the parameters representative of the laboratory conditions (Reynolds & Saric 1986). A free-stream velocity $U^*_\infty = 17$ m/s is chosen. Other parameters are selected to be the values under the standard atmospheric pressure near the ground, namely, $\rho^*_\infty = 1.225\text{kg/m}^3$, $p^*_\infty = 101325\text{Pa}$, $\mu^*_\infty = 1.79 \times 10^{-5}\text{Pa}\cdot\text{s}$ and $c^*_\infty = 340$ m/s, which give a unit Reynolds number $Re^* = 1.1634 \times 10^6/\text{m}$ and Mach number $M = 0.05$. For a given Reynolds number $R = Re^*\delta^*$, there is a corresponding displacement thickness δ^* and the location x^*_c of the scatter, and vice versa.

The imposed steady normal velocity on the wall is taken to be

$$\bar{v}(x, 0) = -\bar{v}_m f(x), \tag{4.4}$$

where $\bar{v}_m$ is the magnitude of the suction velocity with the negative sign indicating suction, and the function $f(x)$ characterizes the distribution. A distribution that is realizable in experiments (Reynolds & Saric 1986) most likely features a top-hat profile, and may be described by

$$f(x; d, \Delta) = \Big\{\tanh[(x - x_c + d/2)/\Delta] - \tanh[(x - x_c - d/2)/\Delta]\Big\}/2, \tag{4.5}$$

where x_c denotes the centre of the suction slot, d is a measure of the slot width and $\Delta \ll d$ characterizes the width in which the velocity increases from zero to $\bar{v}_m$ and vice versa.

Figure 7 shows the characteristics of the steady base flow subject to the suction velocity (4.4) with its distribution given by (4.5). The values of d and $\bar{v}_m$ used correspond to a suction slot with a width $d^* = 29$ mm, velocity $\bar{v}^*_m = 17$ mm/s and a free-stream velocity $U^*_\infty = 17$ m/s, which are representative of wind-tunnel experimental conditions (Reynolds & Saric 1986). The computational domain covers the Reynolds number range $636 < R < 2521$. The local suction produces a distortion to the flow in the regions upstream and downstream of the suction slot. The range of upstream influence is limited; when $R < 1000$ the flow field is almost identical to that of the Blasius boundary layer. However, in the downstream direction the effect of suction extends as far as to $R = 2000$, by which the relaxation to the Blasius flow completes. Near the suction slot ($R_c = 1262$), an appreciable distortion is induced despite a fairly small suction velocity $\bar{v}_m = 0.001$ as can be observed in the contours of the shear dU/dy and the streamlines (figures 7a and b). The fluid in the region below about 40% of the boundary-layer displacement

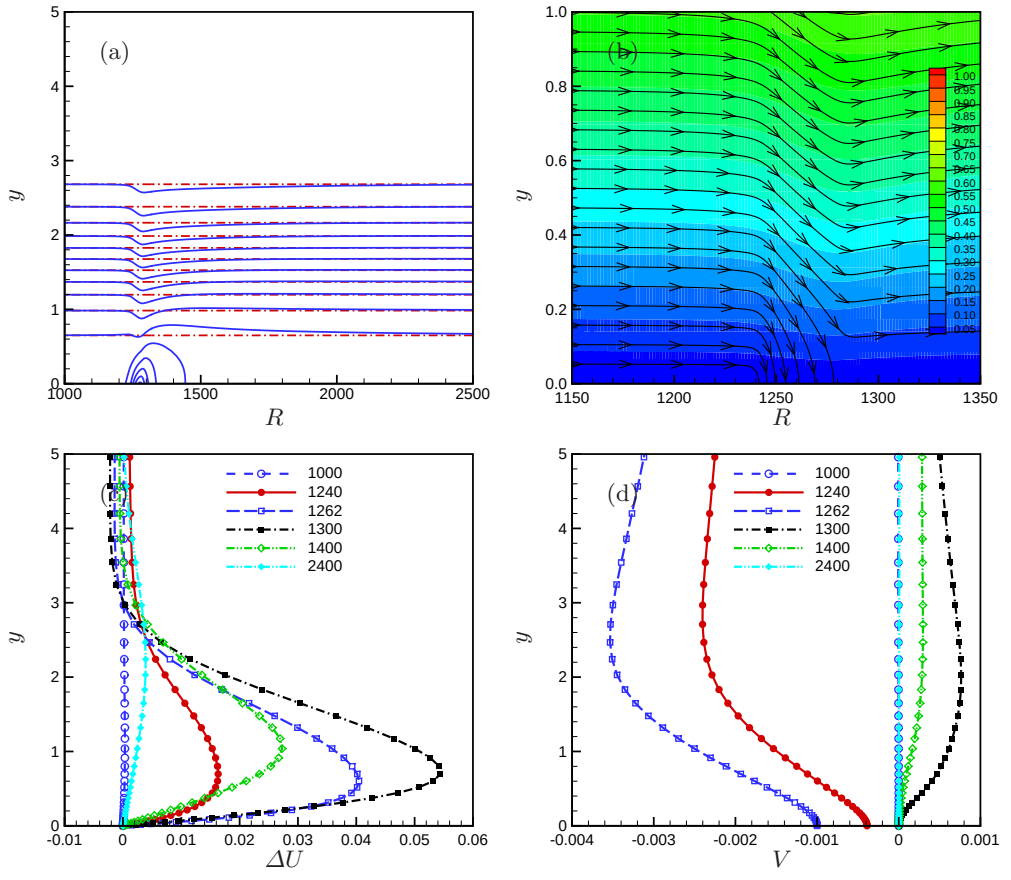

FIGURE 7. The mean-flow distortion induced by a local suction centred at $R_c = 1262$ with the velocity distribution described by (4.4)-(4.5), in which $d = 27$, $\Delta = 2.4$ and $\bar{v}_m = 0.001$. (a) Contours of the shear dU/dy with the dash lines representing the Blasius flow and the solid lines indicating the result with the local suction; (b) Streamlines and the velocity vector field $\mathbf{U}$; (c) Profiles of the streamwise velocity distortion ΔU at different streamwise locations. (d) Profiles of the transverse velocity V at different streamwise locations. (The transverse velocity of the Blasius flow was taken to be zero.)

thickness flows out of the boundary layer through the slot (figure 7b). Figures 7c and d indicate that while the vertical velocity induced in the boundary layer by the suction is comparable with $\bar{v}_m$, the change to the streamwise velocity, which corresponds to flow acceleration, is about 5%, fifty times as large as $\bar{v}_m$. Compared with the unperturbed flow, the distortion is still small, but remarkably it is capable of influencing the oncoming T-S wave substantially as will be shown below.

Figure 8 shows the results obtained by LSA, LST and DNS. Without suction, the T-S mode would evolve following the dot-dashed lines in figure 8a. When the location suction is imposed, the T-S wave is much reduced as figure 8b indicates. In the region over the local suction, which is centred at $R_c = 1262$, there is a sharp decrease of the local growth rate, indicating that the local suction significantly stabilizes the T-S wave. Both LSA and LST predict this stabilizing effect as does the DNS. The predicted amplitude as well as the local growth rate and wavenumber are in good qualitative agreement, but appreciable quantitative differences exist. Interestingly, the predicted transmission

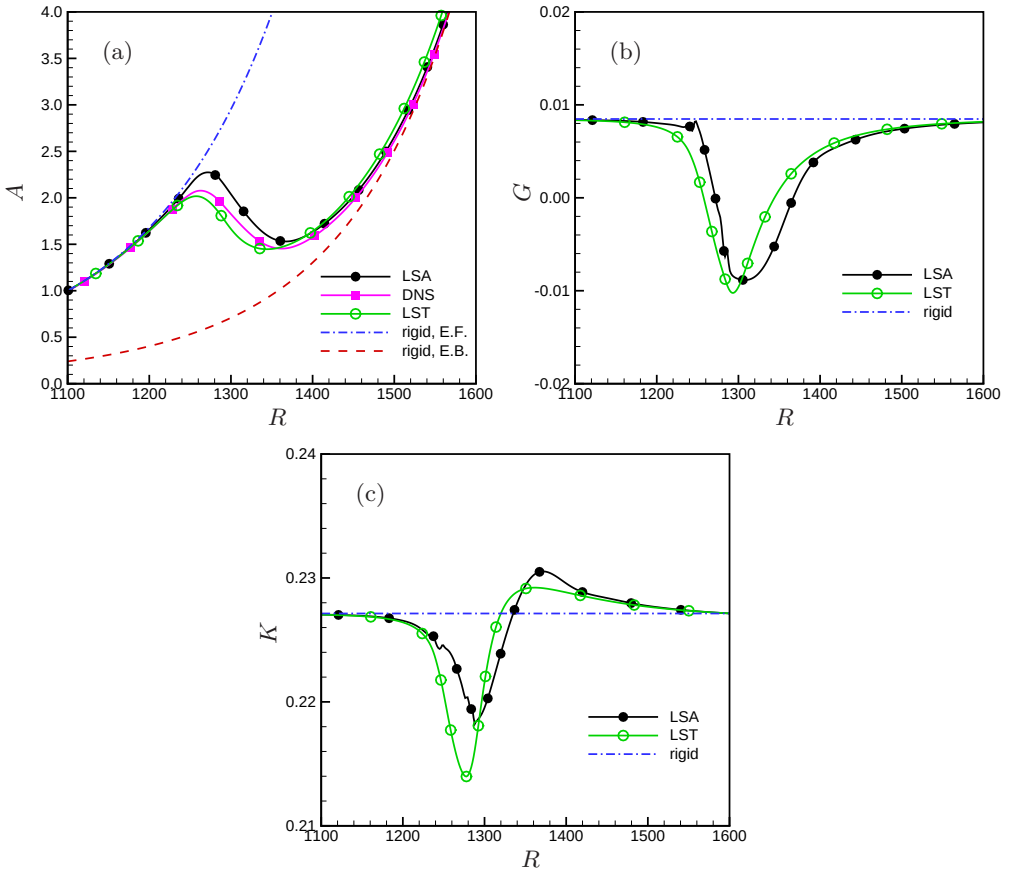

FIGURE 8. The local amplitude A, growth rate G and wavenumber K versus the local Reynolds number R for a T-S wave with frequency $F = 60$ scattered by a local suction centred at $R_c = 1262$ with the slot width $d = 27$, $\Delta = 2.4$ and the maximum suction velocity $\bar{v}_m = 0.001$. The dash-dotted line (labelled as 'rigid, E.F.'): the exponential growth of the incident T-S wave in the absence of suction; the dashed line (labelled as 'rigid, E.B.'): backward extrapolation of the transmitted wave using the growth rate for the rigid wall without suction.

coefficients are near the same: LSA and LST give $Tr = 0.242$ and 0.258 respectively, suggesting that Tr is less sensitive than the local behaviour. It should be stressed that only LSA is the appropriate theory. The close agreement could be explained by observing that even though the width of the suction slot $d = 27$ is rather short, which is about one wavelength of the imposed T-S wave for $R = 1262$ and $F = 60$, the local suction affects the mean flow in a much larger range extending from $R = 1000$ to $R = 2000$, which is nearly $8d$. Furthermore, since the magnitude of the suction velocity is rather small ($\bar{v}_m = 0.001$), the mean flow varies fairly slowly in the streamwise direction. As a result of these, LST may serve as an approximation.

The parameters characterizing the suction are d, $\bar{v}_m$ and Δ, on which the total suction flow rate

$$Q = \bar{v}_m \int_{-\infty}^{\infty} f(x; d, \Delta) dx, \tag{4.6}$$

may depend in general. It is worth noting that for the distribution (4.5), the suction flow

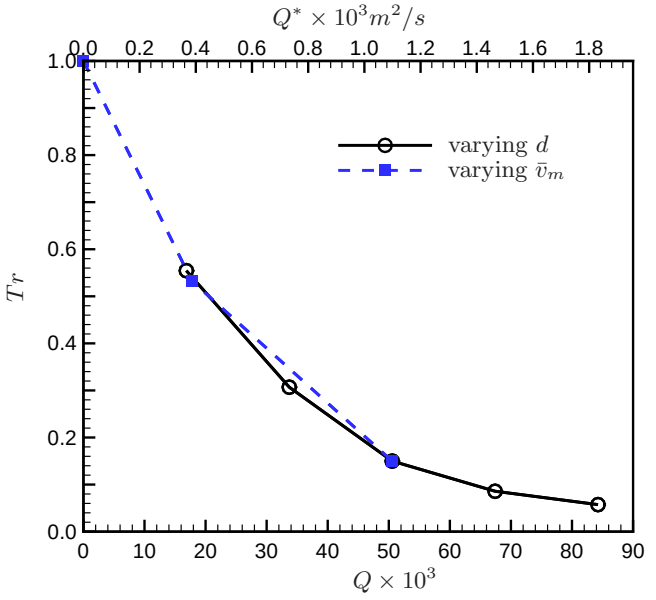

FIGURE 9. Effects of the total suction flow rate Q on the transmission coefficient Tr. The T-S wave has a frequency $F = 25$ and the local suction slot is centred at $R_c = 1339$. The total suction flow rate Q is changed either by varying the suction width d with a fixed suction velocity $v_m^* = 5.7 \times 10^{-3} U_\infty^*$ (circle) or by altering the suction velocity v_m^* with a fixed suction width $d^* = 12.8mm$ (square). The suction length in the spanwise direction is taken to be $0.91m$ as in the wind-tunnel experiment (Reynolds & Saric 1986), and Q^* stands for the dimensional suction flow rate per unit spanwise length of the strip.

rate is

$$Q = \bar{v}_m \, d, \tag{4.7}$$

independent of Δ, and that $\bar{v}(x_c \pm d/2, 0) = -\frac{1}{2}\bar{v}_m \tanh(d/\Delta) \neq 0$. These indicate that d is not the (non-dimensionalised) geometric width of the slot, rather it is the equivalent width that gives the same flux Q if the maximum velocity $\bar{v}_m$ were uniformly distributed over d.

We now exam the role of the suction flow rate Q in scattering and its effect on the transmission coefficient Tr. The value of Q is changed by two ways: by varying the suction width d while holding the suction velocity $\bar{v}_m$ fixed, and alternatively by altering the suction velocity $\bar{v}_m$ with the suction width d fixed. The results in figure 9 show that regardless how Q is varied, the transmission coefficient Tr remains almost the same as long as Q is equal, indicating that the total suction flow rate is the key parameter for the laminar flow control. Tr decreases monotonically with the increase of Q. Furthermore, Tr decreases almost linearly with the increase of Q when $Q < 50 \times 10^{-3}$ (or $Q^* < 1.1 \times 10^{-3} m^2/s$ in the present dimensional setting), and Tr reaches 0.06 as Q rises to 85×10^{-3} (or Q^* rises to $1.8 \times 10^{-3} m^2/s$).

4.3. *Quantitative comparison with experiments*

Finally, we perform calculations for the parameter values pertaining to the four cases (I, II, III and IV) in the experiments of Reynolds & Saric (1986), and make detailed comparisons with the experimental data. In order to be consistent with the experiments, the Reynolds number R in this subsection is based on the boundary-layer thickness defined as $\sqrt{\nu_\infty^* x_c^*/U_\infty^*}$ rather than on the displacement thickness. Case III is considered

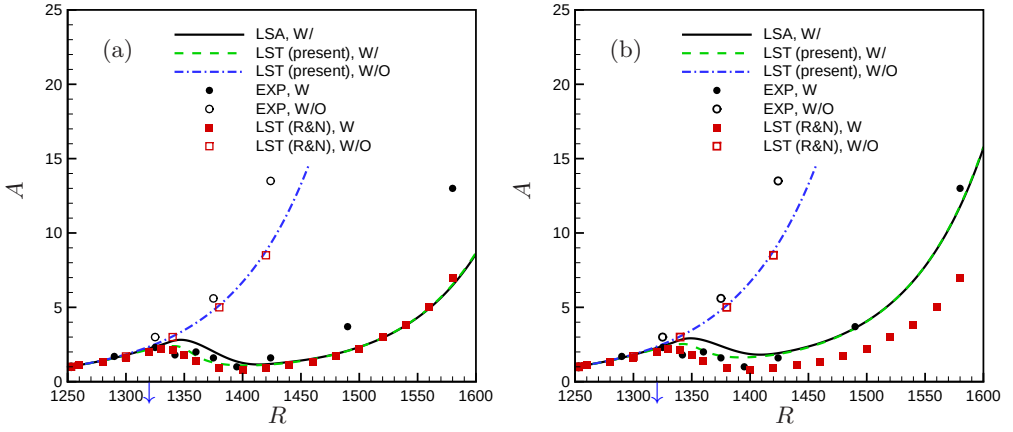

FIGURE 10. The disturbance amplitude vs the local Reynolds number. The parameters come from the suction Case III in the experiments of Reynolds & Saric (1986): suction location $R_c = 1339$, suction velocity $v_m^* = 5.7 \times 10^{-3} U_\infty^*$: (a) suction width $d^* = 16mm$ without correcting the edge effect, (b) equivalent suction width $d^* = 12.8mm$ after accounting for the edge effect. Solid line, LSA; dashed line, LST (present); circle, experiment (Reynolds & Saric 1986); rectangle, LST (R&N) (Reed & Nayfeh 1986). Caption "W/" means "with suction", and caption "W/O" indicates "without suction".

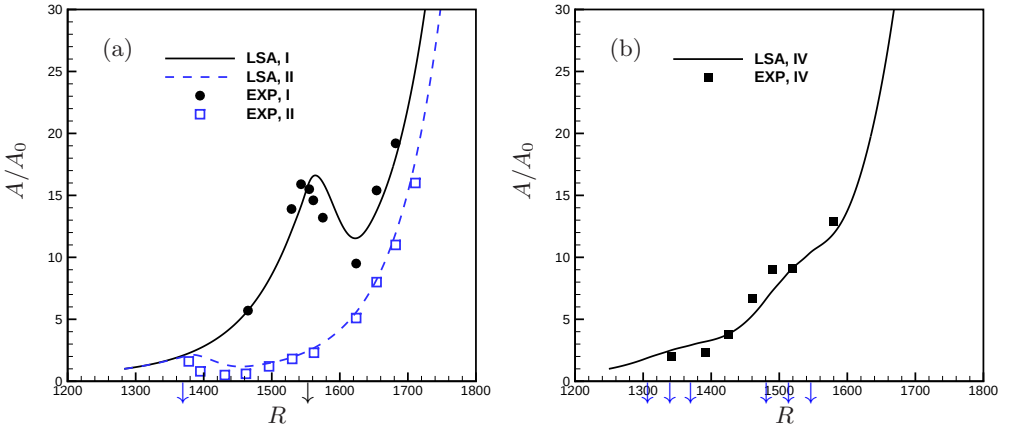

FIGURE 11. The disturbance amplitude versus the local Reynolds number for Cases I, II & IV in the experiments of Reynolds & Saric (Reynolds & Saric 1986): (a) Cases I and II, single suction; (b) Case IV, six suction strips, the locations of which are indicated by arrows in the figure. The width of each suction strip is $d^* = 12.8mm$ with the edge effect accounted for in LSA. Line, LSA (present); symbol, experiment (Reynolds & Saric 1986).

first, where a suction flux of $10^{-3} m^3/s$ through 16mm× 910mm strip was given, and a suction velocity $v_m^* = 5.7 \times 10^{-3} U_\infty^*$ was also quoted. A calculation was first carried out by assuming this to be a uniform (i.e. mean) suction velocity over the geometric width $d^* = 16mm$, and the result is shown in figure 10a. Suction suppresses the T-S wave considerably. Interestingly, the disturbance development predicted by LSA is in good agreement with the prediction by the LST analysis performed by Reed & Nayfeh (1986). In their work, the distorted base flow was calculated by using the linear triple-deck theory, which is based on the large-Reynolds-number assumption. We carried out LST analysis for the base flow computed numerically, which is more accurate. The result

turns out to be virtually the same as that of Reed & Nayfeh (1986). The LSA prediction is a good qualitative agreement with the experimental data. However, an appreciable quantitative difference exists. We find that this is caused by the edge effect of the suction strip. Treating the suction velocity $v_m^* = 5.7 \times 10^{-3} U_\infty^*$ given by Reynolds & Saric (1986) as the mean (uniform) velocity over the entire strip $d^* = 16mm$ leads to a suction flow rate larger than the given value of $10^{-3} m^3/s$, indicating that v_m^* is not the mean value but the peak value instead. Use of this maximum value as the mean suction velocity in LSA and LST caused the discrepancy. The true mean suction velocity must be smaller because of the blocking effect of the slot edges. The latter can be accounted for by a suitably smoothed suction profile (4.5). In order to ensure that the total suction flow rate, the key controlling parameter as the result figure 9 indicates, is the same as that in the experiment, we may either use $d^* = 16mm$ as the equivalent width while reducing v_m^* to Q^*/d^* according to (4.7), or alternatively, take v_m^* as the maximum velocity but choose the equivalent suction width $d^* = Q^*/v_m^* = 12.8mm$, where Q^* is the flux rate per unit spanwise length of the slot. These two treatments lead to the same result as expected. Figure 10b presents the results of LSA and LST calculated after the edge effect is corrected. The prediction by LSA is now in good quantitative agreement with the experiment measurement. The LST result turns out to be just as accurate because for a weak suction the induced distortion varies rather slowly as we observed earlier. In this sense, the success of LST is somewhat fortuitous, and is not expected if the distortion is genuinely abrupt.

Figure 11 shows the evolution of the amplitude obtained by LSA for the Cases I and II of the experiments of Reynolds & Saric (1986), for which the suction slot was centred at $R_c = 1552$ and 1370 respectively, and the T-S wave has the frequency $F = 20$ with its neutral position at $R = 1040$. The experimental measurements are also presented for comparison. As with Case III, the suction width was taken to be $d^* = 12.8mm$ in order to account for the edge effect. A good quantitative agreement between the prediction by LSA and the experimental data can be seen for both cases. The transmission coefficient is found to be 0.15 and 0.11, respectively. The suction strip in Case II is closer to the lower-branch neutral position, which is at $R = 1040$, whereas the suction in Case I is closer to the location of maximum growth, $R = 1650$. The reduction in the T-S wave amplitude is more pronounced than that in Case I, and correspondingly transition would be delayed farther downstream. The result suggests that it is preferable to apply suction in the initial region of growth near the lower branch of the neutral stability curve, instead in the region where the wave is already highly amplified. A further calculation was performed for Case IV, in which the suction is applied through six strips, but the total flux is kept the same as that in the Cases I, II and III. The result is shown in figure 11b, and again the agreement with the experimental data is satisfactory. The transmission coefficient was found to be 0.13, indicating that multi-strip or distributed suction is just as effective as a single strip suction. The latter is however less difficult to deploy in practice.

5. Summary and conclusions

In the present paper, we investigated the effects of abrupt local changes on instability and transition of boundary-layer flows. As the change of interest takes place over a length scale comparable with, or even shorter than, the characteristic wavelength of the instability, the key assumption of LST and PSE that instability waves modulate slowly does not hold, and both LST and PSE fail. Instead, the problem should be formulated as a local scattering problem as was pointed out by Wu & Hogg (2006) and Wu & Dong (2016), where a local scattering approach was presented using the high-Reynolds-

number asymptotic formalism. In the present work, a finite-Reynolds-number formulation was presented. In either case, the abrupt change acts as a scatter. An incident T-S wave propagates downstream and interacts with the strong inhomogeneity caused by the scatter. Downstream of the scatter, the disturbance finally relaxes to a local eigen mode, which is referred to as the transmitted wave. The transmission coefficient, defined as the ratio of the amplitude of the transmitted wave to that of the incident wave, provides a natural characterization of the effect of the abrupt change.

In the local scattering approach, the disturbance is periodic in time as in LST and PSE, but its shape function is allowed to exhibit fast variations in the streamwise direction as well as in the transverse (wall-normal) direction. Formulated in the frequency domain, the scattering is governed by a boundary-value problem consisting of the linearized N-S equations for the perturbation, boundary conditions upstream and downstream of the scatter as well as the boundary conditions on the wall and at infinity. In order to focus on the strong inhomogeneity caused by the local change, the weak non-parallelism of the unperturbed background flow was neglected, and this allowed the scattering to be formulated as an eigenvalue problem, in which the transmission coefficient appears as the eigenvalue as in Wu & Dong (2016). Since the LSA is global and elliptic mathematically, a local scatter can influence the perturbation both upstream and downstream. In contrast, the PSE are parabolic whilst LST only solves the eigenvalue problem, which is specified in terms of the local base flow and local boundary conditions at a given streamwise position. Hence neither can account for any upstream influence. LSA is therefore fundamentally different from LST and PSE. Nevertheless, when the scatter is relatively wide compared with the T-S wavelength or the base flow varies slowly in the streamwise direction, both LST and LSA can give the right solution. This is the case for a local porous panel with a large width d and a small porosity λ_m, and for a local suction with a wide enough slot and a small suction velocity $\bar{v}_m$. However, when the extend of the scatter is comparable with the T-S wavelength, LST gives wrong results.

In order to quantify the effect of the local scatter on stability and transition, the eigenvalue problem is solved numerically to predict the development of the disturbance and the transmission coefficient for the cases of a T-S wave scattered by the abrupt changes due to a local suction and a finite-porous panel interspersing rigid walls. The theoretical prediction of LSA is verified by the direct numerical simulations in time domain. Parametric studies show that a finite porous panel enhances T-S waves and thus plays a destabilizing role. In contrast, a steady local suction suppresses the T-S wave, and the amount of suppression is determined primarily by the mass flux of the suction. A comprehensive comparison of the theoretical predictions with the experimental data was made, and a good quantitative agreement was obtained.

Acknowledgment

This work was supported by the National Natural Science Foundation (Grants 11332007, 11172204, 11672351), the Tianjin Natural Science Foundation (15JCYBJC19500) and an open fund from the State Key Laboratory of Aerodynamics (SKLA201601). The authors would like to thank Professor Jisheng Luo of Tianjin University for valuable discussions.

Appendix A. Computation of the transfer matrix

As was mentioned in the formulation (§2), a transfer matrix **T**, which relates the eigenfunctions of the incident and transmitted instability modes (see (2.30)) needs to

be known in advance. We now show that the existence of this transfer matrix can be established by using the so-called EEV approach for linear instability of weakly non-parallel flows proposed by Huang & Wu (2015). The approach yields the transfer matrix rather naturally.

Let $\bar{\mathbf{Q}}_I$ and $\bar{\mathbf{Q}}_T$ denote the base flow profiles at far upstream and downstream positions, respectively. Then the eigenfunctions of the inlet and outlet, $\tilde{\phi}_I$ and $\tilde{\phi}_T$, can be obtained by solving the eigenvalue problems associated with $\bar{\mathbf{Q}}_I$ and $\bar{\mathbf{Q}}_T$, respectively. In general, $\bar{\mathbf{Q}}_T$ differs from $\bar{\mathbf{Q}}_I$. We may view $\bar{\mathbf{Q}}_T$ as arising through a consequence of a gradual deformation of $\bar{\mathbf{Q}}_I$. This may take place naturally in real physical situations, e.g. the Blasius boundary layer, in which case $\bar{\mathbf{Q}}_I$ evolves into $\bar{\mathbf{Q}}_T$ following the similarity solution. However, not all base-flow properties can be associated naturally with a physical development, and indeed such an association is not necessary. More generally, it is always possible to take a mathematical approach and represent the intermediate state between $\bar{\mathbf{Q}}_I$ and $\bar{\mathbf{Q}}_T$ as

$$\bar{\mathbf{Q}}(x) = \bar{\mathbf{Q}}_I + (\bar{\mathbf{Q}}_T - \bar{\mathbf{Q}}_I)g(x), \tag{A 1}$$

where $g(x)$ is the tapering function chosen to satisfy $g \to 0$ as $x \to -\infty$ and $g \to 1$ as $x \to \infty$. It should be stressed that $g(x)$ is a function slowly varying with x, unlike $f(x)$ describing the scatter, which is a fast function of x. Since $\bar{\mathbf{Q}}$ varies slowly with x, so does its corresponding eigenvector $\tilde{\phi}$.

In the EEV approach (Huang & Wu 2015), the local eigenfunction in the vicinity of an arbitrary streamwise location x_a is expanded as a Taylor series

$$\tilde{\phi}(x_a + \triangle x) = a\Big[\tilde{\phi}_0(x_a, y) + \triangle x\tilde{\phi}_1(x_a, y) + \frac{1}{2}\triangle x^2\tilde{\phi}_2(x_a, y) + \cdots\Big], \tag{A 2}$$

where a is a coefficient to to ensure the eigenfunction $\tilde{\phi}(x_a+\triangle x)$ has a norm of unity. An extended eigenvalue problem arises with the wavenumber α and $(\tilde{\phi}_0, \tilde{\phi}_1, \tilde{\phi}_2)^T$ appearing as the eigenfunction (eigenvector). Solving that eigenvalue problem, one obtains not only the local eigenvalue α and its corresponding eigenfunction $(\tilde{\phi}_0, \tilde{\phi}_1, \tilde{\phi}_2)^T$, but also the matrices $\mathbf{T}_1$ and $\mathbf{T}_2$, where

$$\tilde{\phi}_1 = \mathbf{T}_1\tilde{\phi}_0, \quad \tilde{\phi}_2 = \mathbf{T}_2\tilde{\phi}_0. \tag{A 3}$$

It follows that the eigenfunction in the vicinity of an arbitrary point x_a is linked via the relation

$$\tilde{\phi}(x_a + \triangle x) = a\Big[\mathbf{I} + \triangle x\mathbf{T}_1 + \frac{1}{2}\triangle x^2\mathbf{T}_2 + \cdots\Big]\tilde{\phi}_0 \equiv \tilde{\mathbf{T}}(x_a)\tilde{\phi}_0(x_a, y), \tag{A 4}$$

where the local transfer matrix $\tilde{\mathbf{T}}(x_a)$ is given by

$$\tilde{\mathbf{T}}(x_a) = a\Big[\mathbf{I} + \triangle x\mathbf{T}_1 + \frac{1}{2}\triangle x^2\mathbf{T}_2 + \cdots\Big]. \tag{A 5}$$

By carrying out the EEV calculation for the intermediate base state and/or boundary conditions, represented by $\bar{\mathbf{Q}}$ in (A 1), at each mesh point x_i between the inlet x_0 and outlet x_n, one obtains the local transfer matrix $\mathbf{T}(x_i)$ with $i = 1, 2, \ldots, n$. The product of the local transfer matrices then gives the required global transfer matrix,

$$\mathbf{T} = \prod_{i=1}^{n} \tilde{\mathbf{T}}(x_i). \tag{A 6}$$

In the discretized form, the two eigenvectors at the inlet and outlet, $\tilde{\phi}_I$ and $\tilde{\phi}_T$, can be related via a transfer matrix $\tilde{\mathbf{T}}$ such that $\tilde{\phi}_T = \mathbf{T}\tilde{\phi}_I$. If $\bar{\mathbf{Q}}_T$ is identical to $\bar{\mathbf{Q}}_I$, which

Tapering function	D	$\triangle x$	$\lvert\tilde{\phi}_T - \mathbf{T}\tilde{\phi}_I\rvert_\infty$	$\lvert\phi_0 - \tilde{\phi}_I\rvert_\infty$	$\lvert\phi_n/\lvert\phi_n\rvert_\infty - \tilde{\phi}_T\rvert_\infty$	Tr
sin	300	0.5	2.44E-5	6.59E-7	3.19E-6	1.79197362
sin	300	5.0	3.87E-5	6.60E-7	3.29E-6	1.79199132
tanh	40	0.5	4.57E-6	1.45E-7	4.51E-6	1.79172500
tanh	40	5.0	7.00E-6	1.45E-7	5.21E-6	1.79170054

TABLE 1. Test of tapering functions

is the case for an isolated scatter with the unperturbed base-flow being assumed to be parallel, then the transmission matrix $\mathbf{T}$ is the unit matrix $\mathbf{I}$.

Two forms of tapering function were adopted and tested in this paper. The first is defined as

$$g(x) = \begin{cases} 0 & x < -D/2, \\ \big[\sin(2\pi x/D) + 1\big]/2 & |x| \leqslant D/2, \\ 1 & x > D/2, \end{cases} \tag{A 7}$$

and the second is

$$g(x) = \big[\tanh(x/D) + 1\big]/2, \tag{A 8}$$

where D is a measure of the length of the gradual deformation, and is chosen to be much greater than the width d (or Δ) of the scatter. Using these two tapering functions (referred to as sin and tanh respectively), we performed the calculations for the case of a T-S wave with a frequency $F = 60$ and wavelength $\lambda_{TS} = 27$ being scattered by a rigid-porous junction at $R_c = 1262$ with $\lambda_m = 1$ and $\varphi = 0°$. Two mesh sizes are used. The results are displayed in table 1, in which $\tilde{\phi}_I$ and $\tilde{\phi}_T$ are the local eigenfunctions at the inlet and outlet respectively, while ϕ_0 is the eigenfunction of (3.20), ϕ_n is the solution in (3.18) . The accuracy of the transfer matrix $\mathbf{T}$ can be measured by the maximum error, $|\tilde{\phi}_T - \mathbf{T}\tilde{\phi}_I|_\infty$, where the norm is defined as

$$\big|\cdot\big|_\infty = \max_y |\cdot|. \tag{A 9}$$

The consistency and accuracy of the solution may be measured by the maximum errors of $(\phi_0 - \tilde{\phi}_I)$ and $(\phi_n/|\phi_n|_\infty - \tilde{\phi}_T)$, which characterize how well the scattering solution matches with the local instability modes upstream and downstream respectively. As is indicated in table 1, for both tapering functions and mesh sizes, all the errors are fairly small. The predicted transmission coefficient Tr is independent of the choice of the tapering function and the mesh size. This was also found to be true of the disturbance development.

REFERENCES

AIRIAU, C., BOTTARO, A., WALTHER, S. & LEGENDRE, D. 2003 A methodology for optimal laminar flow control: Application to the damping of Tollmien-Schlichting waves in a boundary layer. *Phys. Fluids* **15** (5), 1131–1145.

BABUCKE, A., KLOKER, M. & RIST, U. 2008 DNS of a plane mixing layer for the investigation of sound generation mechanisms. *Comput. Fluids* **37**, 360–368.

BERTOLOTTI, F. P., HERBERT, TH. & SPALART, P. R. 1992 Linear and nonlinear stability of the Blasius boundary layer. *J. Fluid Mech.* **242**, 441–474.

CEBECI, T. & EGAN, D. A. 1989 Prediction of transition due to isolated roughness. *AIAA J.* **27** (7), 870–875.

Chang, C.-L. & Malik, M. R. 1994 Oblique-mode breakdown and secondary instability in supersonic boundary layers. *J. Fluid Mech.* **273**, 323–360.

Choudhari, M. & Duck, P. W. 1996 Nonlinear excitation of inviscid stationary vortex instabilities in a boundary-layer flow. In *Proceeding of IUTAM Symposium on Nonlinear Instability and Transition in Three-Dimensional Boundary Layers, Manchester, U.K., 17–20 July 1995* (ed. P. W. Duck & H. Philip), pp. 409–422. Dordrecht: Springer Netherlands.

Colonius, T. 2004 Modelling artificial boundary conditions for compressible flow. *Annu. Rev. Fluid Mech.* **36** (1), 315–345.

Darcy, H. 1856 *Les Fontaines Publiques de la Ville de Dijon*. Paris: Dalmont.

Edelmann, C. A. & Rist, U. 2013 Impact of forward-facing steps on laminar-turbulent transition in transonic flows without pressure gradient. *AIAA Paper 2013-0080* .

Fasel, H. 1976 Investigation of the stability of boundary layers by a finte-difference model of the Navier-Stokes equations. *J. Fluid Mech.* **78**, 355–383.

Fedorov, A. V. 2011 Transition and stability of high-speed boundary layers. *Annu. Rev. Fluid Mech.* **43** (1), 79–95.

Fong, K. D., Wang, X. W. & Zhong, X. L. 2013 Stabilization of hypersonic boundary layer by 2-D surface roughness. *AIAA Paper 2013-2985* .

Fujii, K. 2006 Experiment of the two-dimensional roughness effect on hypersonic boundary-layer transition. *AIAA J.* **43** (4), 731–738.

Gaster, M. 1974 On the effects of boundary-layer growth on flow stability. *J. Fluid Mech.* **66** (03), 465–480.

Herbert, T. 1997 Parabolized stability equations. *Annu. Rev. Fluid Mech.* **29** (1), 245–283.

Huang, Z. F., Cao, W. & Zhou, H. 2005*a* The mechanism of breakdown in laminar-turbulent transition of a supersonic boundary layer on a flat plate —— temporal mode. *Sci. China Ser. G* **48**, 614–625, 10.1360/142005-19.

Huang, Z. F. & Wu, X. 2015 A non-perturbative approach to spatial instability of weakly non-parallel shear flows. *Phys. Fluids* **27** (054102), 1–21.

Huang, Z. F., Zhou, H. & Luo, J. S. 2005*b* Direct numerical simulation of a supersonic turbulent boundary layer on a flat plate and its analysis. *Sci. China Ser. G* **48**, 626–640, 10.1360/142005-184.

Kleiser, L. & Zang, T. A. 1991 Direct numerical simulation of transition in wall-bounded shear flows. *Annu. Rev. Fluid Mech.* **23** (1), 495–537.

Kloker, M., Konzelmann, U. & Fasel, H. 1993 Outflow boundary conditions for spatial Navier-Stokes simulations of transitional boundary layers. *AIAA J.* **31** (4), 620–628.

Kurz, H. & Kloker, M. J. 2014 Receptivity of a swept-wing boundary layer to micron-sized discrete roughness elements. *J. Fluid Mech.* **755**, 62–82.

Malik, M. R. 1990 Finite difference solution of the compressible stability eigenvalue problem. *Tech. Rep.* 16572. NASA Tech. Rep.

Malik, M. R., Li, F. & Chang, C.-L. 1994 Crossflow disturbances in three-dimensional boundary layers: nonlinear development, wave interaction and secondary instability. *J. Fluid Mech.* **268**, 1–36.

Marxen, O., Iaccarino, G. & Shaqfeh, E.S. G. 2010 Disturbance evolution in a Mach 4.8 boundary layer with two-dimensional roughness-induced separation and shock. *J. Fluid Mech.* **648**, 436–469.

Masad, J. A. 1995 Transition in flow over heat-transfer strips. *Phys. Fluids* **7** (9), 2163–2174.

Masad, J. A. & Nayfeh, A. H. 1992 Laminar flow control of subsonic boundary layers by suction and heat-transfer strips. *Phys. Fluids* **4** (6), 1259–1272.

Meitz, H. L. & Fasel, H. 2000 A compact-difference scheme for the Navier-Stokes equaions in vorticity-velocity formulation. *J. Comput. Phys.* **157** (1), 371–403.

Nayfeh, A. H. & Abu-Khajeel, H. T. 1996 Effect of a hump on the stability of subsonic boundary layers over an airfoil. *Int. J. Eng. Sci.* **34** (6), 599–628.

Nayfeh, A. H., Ragab, S. A. & AlMaaitah, A. A. 1988 Effect of bulges on the stability of boundary layers. *Phys. Fluids* **31** (4), 795–806.

Nayfeh, A. H. & Reed, H. L. 1985 Stability of flow over axisymmetric bodies with porous suction strips. *Phys. Fluids* **28** (10), 2990–2998.

Park, D. & Park, S. O. 2013 Linear and non-linear stability analysis of incompressible boundary layer over a two-dimensional hump. *Comput. Fluids* **73**, 80–96.

Pralits, J. O. & Hanifi, A. 2003 Optimization of steady suction for disturbance control on infinite swept wings. *Phys. Fluids* **15** (9), 2756–2772.

Pralits, J. O., Hanifi, A. & Henningson, D. S. 2002 Adjoint-based optimization of steady suction for disturbance control in incompressible flows. *J. Fluid Mech.* **467**, 129–161.

Reed, H. L. & Nayfeh, A. H. 1986 Numerical-perturbation technique for stability of flat-plate boundary layers with suction. *AIAA J.* **24** (2), 208–214.

Reed, H. L., Saric, W. S. & Arnal, D. 1996 Linear stability theory applied to boundary layers. *Annu. Rev. Fluid Mech.* **28** (1), 389–428.

Reshotko, E. 1976 Boundary-layer stability and transition. *Annu. Rev. Fluid Mech.* **8** (1), 311–349.

Reynolds, G. A. & Saric, W. S. 1986 Experiments on the stability of the flat-plate boundary layer with suction. *AIAA J.* **24** (2), 202–207.

Rist, U. & Fasel, H. 1995 Direct numerical simulation of controlled transition in flat-plate boundary layer. *J. Fluid Mech.* **298**, 211–248.

Wang, X. W. & Zhong, X. L. 2012 The stabilization of a hypersonic boundary layer using local sections of porous coating. *Phys. Fluids* **24** (034105), 1–28.

Wie, Y. & Malik, M. R. 1998 Effect of surface waviness on boundary-layer transition in two-dimensional flow. *Comput. Fluids* **27** (2), 157–181.

Worner, A., Rist, U. & Wagner, S. 2003 Humps/steps influence on stability characteristics of two-dimensional laminar boundary layer. *AIAA J.* **41** (2), 192–197.

Wu, X. & Dong, M. 2016 A local scattering theory for the effects of isolated roughness on boundary-layer instability and transition: transmission coefficient as an eigenvalue. *J. Fluid Mech.* **794**, 68–108.

Wu, X. & Hogg, L. W. 2006 Acoustic radiation of Tollmien-Schlichting waves as they undergo rapid distortion. *J. Fluid Mech.* **550**, 307–347.

Xu, H., Sherwin, S. J., Hall, P. & Wu, X. 2016 The behaviour of Tollmien-Schlichting waves undergoing small-scale localised distortions. *J. Fluid Mech.* **792**, 499–525.

Zhong, X. L. & Wang, X. W. 2012 Direct numerical simulation on the receptivity, instability, and transition of hypersonic boundary layers. *Annu. Rev. Fluid Mech.* **44** (1), 527–561.